International Journal of Solids and Structures 316 (2025) 113376

Contents lists available at ScienceDirect

International Journal of Solids and Structures

journal homepage: www.elsevier.com/locate/ijsolstr

Eulerian rates of elastic incompatibilities for crystal plasticity applied to size-dependent hardening in finite bending

Lorenzo Bardella [a,*], M.B. Rubin [b], Andrea Panteghini [a]

[a] Department of Civil, Environmental, Architectural Engineering and Mathematics, University of Brescia, Italy
[b] Faculty of Mechanical Engineering, Technion-Israel Institute of Technology, 32000, Haifa, Israel

ARTICLE INFO

Keywords:
Crystal plasticity
Elastic incompatibility
Eulerian formulation
Large deformation
Small-scale metal plasticity
Uniform bending
Size-effect

ABSTRACT

By following the work in (Rubin and Bardella, 2024), this investigation develops measures of rates of elastic incompatibilities, denoted as R_{ij}, for crystal plasticity. This effort relies on Eulerian constitutive equations for finite-deformation anisotropic elastoplasticity governed by the evolution of microstructural material vectors. The rates R_{ij} depend on the crystallography as the latter enters the rate of plasticity $\mathbf{L}_p$ and the R_{ij} are obtained by evaluating the opposite of the current curl of $\mathbf{L}_p$ relative to the microstructural vectors. Each component of R_{ij} is invariant under superposed rigid body motions, such that it can be independently employed in the constitutive equations. In crystal plasticity, the adopted Eulerian framework allows for singling out in R_{ij} the contributions due to rates of densities of geometrically necessary dislocations and to the elastic distortion of the crystal lattice. In this work, R_{ij} are used to enhance the hardening, which is applied to the size-dependent material response of structurally thick circular sectors subjected to uniform large-deformation bending.

1. Introduction

This work is a continuation of (Rubin and Bardella, 2024), where Eulerian rates of elastic incompatibilities are developed. The adopted finite-deformation Eulerian framework relies on the evolution equations for the material microstructural vectors (Rubin, 1994)

$$\dot{\mathbf{m}}_i = (\mathbf{L} - \mathbf{L}_p)\mathbf{m}_i\,, \tag{1}$$

where $\mathbf{m}_i$, $i = 1, 2, 3$, constitute a triad of linearly independent vectors that are orthonormal in a Reference Lattice State (RLS) with zero stress and reference temperature; moreover, $\dot{(\,)}$ indicates the material time derivative, $\mathbf{L}$ is the total velocity gradient, and $\mathbf{L}_p$ is the second-order tensor *constitutively* defining the plastic rate. The evolution of the triad $\mathbf{m}_i$ can characterize elastic deformations and changes in anisotropic orientations from the RLS in any material, including any anisotropy and microstructure, such that it also determines the Cauchy stress $\mathbf{T}$ in the current state. Hence, the vectors $\mathbf{m}_i$ are internal state variables (Onat, 1968) that, in the current configuration, are assumed to be measurable. In fact, in the Eulerian formulation followed here, the constitutive equations must be functions of the values of state variables in the current configuration. Hence, the total deformation gradient $\mathbf{F}$ may not be a state variable in this formulation, as it depends on an arbitrary choice of a reference state, although it admits Lagrangian and Eulerian forms (Rubin, 2012).

Naturally, elastic incompatibility is a Lagrangian notion as it requires the definition of elastic deformation between an initial and the current configurations. By confining attention to simply connected regions, this notion can be discussed through the use of a Nye-Kröner-like elastic tensor $\boldsymbol{\alpha}_e$ (Nye, 1953; Kröner, 1962), which measures elastic incompatibility from the initial configuration to the current configuration. Rubin and Bardella (2024) show that, by taking coincident initial and current configurations, the instantaneous elastic incompatibility rate reduces to

$$\dot{\boldsymbol{\alpha}}_e = -\mathrm{curl}(\mathbf{L}_p)\,, \tag{2}$$

where the curl is taken with respect to the current position $\mathbf{x}$ of a material point located at $\mathbf{X}$, at time $t = 0$, in the initial configuration, with the one-to-one mapping

$$\mathbf{x} = \mathbf{x}(\mathbf{X}, t)\,.$$

Consequently, assuming suitable smoothness, $\dot{\boldsymbol{\alpha}}_e = \mathbf{0}$ at t implies that, at that instant, the instantaneous rate of elastic incompatibility vanishes, which means that, at that instant, the instantaneous rate of elastic deformation is compatible. Note that the expression in Eq. (2) is obtained in (Rubin and Bardella, 2024) from a time-integrable evolution equation that is invariant under superposed rigid body motions (SRBM). However, since Eq. (2) is evaluated under the condition that the initial

* Corresponding author.
E-mail addresses: lorenzo.bardella@ing.unibs.it (L. Bardella), mbrubin@tx.technion.ac.il (M.B. Rubin), andrea.panteghini@unibs.it (A. Panteghini).

https://doi.org/10.1016/j.ijsolstr.2025.113376
Received 26 February 2025; Received in revised form 1 April 2025; Accepted 3 April 2025
Available online 16 April 2025

and current configurations coincide, it represents the instantaneous rate of elastic incompatibility and cannot be integrated as a tensorial quantity.

Specifically, Rubin and Bardella (2024) define the Eulerian rates of elastic incompatibilities for finite deformations as

$$R_{ij} = -\mathrm{curl}(\mathbf{L}_p)\cdot(\mathbf{m}'_i\otimes\mathbf{m}'_j)\,, \tag{3}$$

where $\mathbf{m}'_i$ denotes the distortional part of the microstructural vectors, which are obtained as

$$\mathbf{m}'_i = J_e^{-1/3}\mathbf{m}_i\,,\quad J_e = \mathbf{m}_1\times\mathbf{m}_2\cdot\mathbf{m}_3 > 0\,, \tag{4}$$

where J_e is the elastic dilatation.[1]

The distortional microstructural vectors satisfy

$$\dot{\mathbf{m}}'_i = (\mathbf{L}'' - \mathbf{L}''_p)\mathbf{m}'_i\,, \tag{5}$$

with $(\,)''$ denoting the deviatoric part of a second-order tensor, such that

$$\mathbf{L}'' = \mathbf{L} - \frac{1}{3}\mathrm{tr}(\mathbf{L})\mathbf{I}\,, \tag{6}$$

In (Rubin and Bardella, 2024) it is demonstrated that each component of the Eulerian rates of elastic incompatibilities R_{ij} as defined in Eq. (3) is invariant under SRBM. Therefore, any combination of the components of R_{ij} can be used in Eulerian anisotropic constitutive equations (Rubin, 2012, 2021). In fact, the rates R_{ij} are independent of arbitrary choices of reference and intermediate configurations as well as total and plastic deformation measures, which instead affect definitions of the Nye-Kröner-like tensor in finite-deformation theories relying on the multiplicative decomposition of the total deformation gradient into elastic and plastic contributions (Bilby et al., 1957; Kröner, 1959; Lee, 1969), $\mathbf{F} = \mathbf{F}_e\mathbf{F}_p$. In such a context, there are actually several proposals for the measure of densities of GNDs, as for instance reported and discussed by Cermelli and Gurtin (2001).

It is further noted that R_{ij} are highly nonlinear fields for their quadratic dependence on $\mathbf{m}'_i$, which in turn depend on the loading history, likewise $\mathbf{L}_p$. This notwithstanding, under small strains and rotations, the definition of R_{ij} is consistent with the negative rate of the Nye-Kröner tensor (Nye, 1953; Kröner, 1962). Physically, the Nye-Kröner tensor characterizes densities of geometrically necessary dislocations (GNDs) in a continuum framework for metal plasticity (Ashby, 1970; Fleck and Hutchinson, 1997; Arsenlis and Parks, 1999). Because of this, the Nye-Kröner tensor is also denoted as the dislocation density tensor.

The foregoing arguments support the use of R_{ij} as an adequate quantity to enhance the Eulerian hardening equations to predict size-effects in large-deformation metal plasticity at the microscale. Remarkably, R_{ij} can be used to define incompatibility-dependent fields that allow for either full or partial recovery of the hardening associated with the size dependence, which has a connection with the meaning of GNDs in continuum metal plasticity, also accounting for the dissipation associated with dislocations' motion (Ashby, 1970; Needleman, 2024). This has been done in (Rubin and Bardella, 2024) by focusing on phenomenological plasticity. This kind of effort, if contextualized in the literature on strain-gradient plasticity (SGP), leads to a lower-order theory, because of the absence of higher-order balance equations and higher-order boundary conditions (Acharya and Bassani, 2000; Niordson and Hutchinson, 2003).

[1] About the notation, $\cdot$, $\otimes$, and $\times$ denote, respectively, the inner, the tensor, and the vector products. Specifically, $\mathbf{A}\cdot\mathbf{B}$ indicates the inner product between the two second-order tensors $\mathbf{A}$ and $\mathbf{B}$ and is such that $\mathbf{A}\cdot\mathbf{B} = \mathrm{tr}(\mathbf{A}\mathbf{B}^T)$, in which $\mathrm{tr}(\mathbf{A}) = \mathbf{A}\cdot\mathbf{I}$ is the trace of $\mathbf{A}$ and $\mathbf{I}$ is the second-order identity tensor. Also, by using a fixed orthonormal rectangular Cartesian triad $\mathbf{e}_i$, curl $\mathbf{L}$ is defined so that $(\mathrm{curl}\,\mathbf{L})\cdot(\mathbf{e}_i\otimes\mathbf{e}_j) \equiv \epsilon_{jkl}\partial \mathrm{L}_{il}/\partial \mathrm{x}_k$, with $\epsilon_{ijk} = (i-j)(j-k)(k-i)/2$ indicating the Ricci-Curbastro third-order tensor and $\mathrm{L}_{ij} = \mathbf{L}\cdot(\mathbf{e}_i\otimes\mathbf{e}_j)$, $\mathrm{x}_i = \mathbf{x}\cdot\mathbf{e}_i$. Moreover, Einstein's summation convention is adopted for repeated indices.

The main novelty of this investigation is the application of the foregoing concepts to crystal plasticity. As developed in Section 2, one characterizing feature of the Eulerian approach is that the crystallographic directions evolve with the elastic distortion of the crystal lattice. Specifically, curl($\mathbf{L}_p$) includes two distinct contributions, which can be ascribed to the rates of the densities of GNDs and to the elastic distortion of the crystal lattice. The influence of the elastic deformation on the distortion of the crystallographic slip systems is discussed, for instance, by Asaro (1983) within the context of the multiplicative formulation of elastoplastic response. However, the influence on the incompatibility of the elastic deformation of the crystal lattice is not clear in formulations based on $\mathbf{F} = \mathbf{F}_e\mathbf{F}_p$ and using a Nye-Kröner-like tensor to include size-dependence, because in these formulations the crystallographic directions are held constant as defined either in the intermediate configuration (Cermelli and Gurtin, 2001; Zecevic et al., 2023) or in the reference configuration (Haouala et al., 2020). Additionally, the plastically convected rate of the Nye-Kröner-like tensor developed by (Gurtin, 2006) depends only on contributions due to rates of pure densities of GNDs.

In Section 3, presenting the proposed Eulerian constitutive equations for rate-independent crystal plasticity, the rates R_{ij} are employed to enhance the conventional hardening to obtain a size-dependent hardening. Notably, the resulting size-dependence also introduces some latent hardening. This constitutive framework is applied in Section 4 to predict the large-deformation response of circular sectors subjected to uniform bending, i.e. bending without shear, thus ensuring axial symmetry of the deformed configuration. These sectors are structurally thick, meaning for instance that, in general, the radial stress may not be neglected in comparison to the circumferential stress, although the former vanishes at the inner and outer radii due to the boundary conditions. Specifically, both the purely elastic and elastoplastic responses are studied in detail, such that their comparison helps to better understand this highly nonlinear problem.

The bending problem is an interesting benchmark problem for size-dependent elastoplasticity theories since the pivotal experiments performed by Stölken and Evans (1998), which, remarkably, involve extremely large deformations. This benchmark problem has been studied in several contributions to test SGP theories. For instance, Engelen et al. (2006) adopted the uniform bending problem to discuss differences in the predictions of earlier SGP theories. Later, Idiart et al. (2009) and Martínez-Pañeda et al. (2016) studied this benchmark problem by applying, respectively, the SGP theories of Gudmundson (2004) and Gurtin (2004), the latter using, as higher-order primal variable, the Nye-Kröner dislocation density tensor. However, it is remarked that all these applications of various SGP theories restrict attention to small deformations. Notably, the bending problem is suitable to discuss the results of the proposed lower-order theory of strain gradient crystal plasticity (Acharya and Bassani, 2000) because it does not need higher-order boundary conditions to trigger gradients of plastic deformation rates.

Concluding remarks are presented in Section 5, where it is highlighted that this study demonstrates the importance of the two contributions to curl($\mathbf{L}_p$) due to rates of GNDs densities and to the elastic distortion of the crystal lattice.

2. Eulerian rates of elastic incompatibilities in crystal plasticity

Crystal plasticity models rely on a finite number N of slip systems in the crystal, each system I being able to develop a plastic slip rate ${}_I\Gamma$ and characterized by a plane with unit normal ${}_I\mathbf{n}$ and unit slip direction ${}_I\mathbf{s}$ in that plane, with ${}_I\mathbf{s}\cdot{}_I\mathbf{n} = 0$ in the current configuration (Rice, 1971). Therefore, the plastic rate $\mathbf{L}_p$ in the current configuration is defined by

$$\mathbf{L}_p = \sum_{I=1}^{N} {}_I\Gamma\,{}_I\mathbf{s}\otimes{}_I\mathbf{n}\,. \tag{7}$$

Since ${}_I\mathbf{s}\cdot{}_I\mathbf{n}=0$, Eq. (7) for $\mathbf{L}_p$ is applicable to isochoric metal plasticity, being consistent with $\mathrm{tr}(\mathbf{L}_p)=0$, such that, henceforth

$$\mathbf{L}_p \equiv \mathbf{L}_p'' \,.$$

Also, N and the relative orientations of the slip systems depend on the metal crystallography (see, e.g., Hull and Bacon, 2001, and references therein).

The plastic deformation and spin rates directly come from Eqs. (7) and have the forms

$$\begin{aligned}\mathbf{D}_p &\equiv \mathbf{D}_p'' = \frac{1}{2}(\mathbf{L}_p+\mathbf{L}_p^T) = \sum_{I=1}^{N}\frac{{}_I\Gamma}{2}({}_I\mathbf{s}\otimes{}_I\mathbf{n}+{}_I\mathbf{n}\otimes{}_I\mathbf{s})\,,\\ \mathbf{W}_p &= \frac{1}{2}(\mathbf{L}_p-\mathbf{L}_p^T) = \sum_{I=1}^{N}\frac{{}_I\Gamma}{2}({}_I\mathbf{s}\otimes{}_I\mathbf{n}-{}_I\mathbf{n}\otimes{}_I\mathbf{s})\,.\end{aligned} \tag{8}$$

In the adopted Eulerian framework, the crystallographic directions in the current state are written in terms of the elastic distortional microstructural vectors $\mathbf{m}_i'$ in Eq. (5), by specifying (Rubin, 2021, Sec. 5.13)

$$\begin{aligned}&{}_I\mathbf{n} = \frac{{}_In_i\mathbf{m}^{i\prime}}{|{}_In_j\mathbf{m}^{j\prime}|}\,,\quad {}_I\mathbf{s} = \frac{{}_Is^i\mathbf{m}_i'}{|{}_Is^j\mathbf{m}_j'|}\,,\\ &{}_In_i\,{}_In_i = 1\,,\quad {}_Is^i\,{}_Is^i = 1\,,\quad {}_In_i\,{}_Is^i = 0\,,\end{aligned} \tag{9}$$

where there is no sum on the repeated index I and the reciprocal distortional vectors $\mathbf{m}^{i\prime}$ are defined as

$$\begin{aligned}&\mathbf{m}^{1\prime}=\mathbf{m}_2'\times\mathbf{m}_3'\,,\quad \mathbf{m}^{2\prime}=\mathbf{m}_3'\times\mathbf{m}_1'\,,\quad \mathbf{m}^{3\prime}=\mathbf{m}_1'\times\mathbf{m}_2'\,,\\ &\mathbf{m}_i'\cdot\mathbf{m}^{j\prime}=\delta_i^j\,,\quad \mathbf{m}_j'\otimes\mathbf{m}^{j\prime}=\mathbf{I}\,,\end{aligned} \tag{10}$$

with δ_i^j denoting the mixed Kronecker delta. Importantly, in Eq. (9) the components ${}_In_i$ of ${}_I\mathbf{n}$ and the components ${}_Is^i$ of ${}_I\mathbf{s}$ are constants that are defined in the RLS, where $\mathbf{m}_i'=\mathbf{m}^{i\prime}$ are orthonormal unit vectors.

Eq. (9) simply states that the crystallographic directions follow the crystal lattice, which is subject to elastic deformation.

Moreover, taking the time derivative of the fourth relation in Eq. (10) and using Eq. (5) yields

$$\dot{\mathbf{m}}^{i\prime} = -(\mathbf{L}''-\mathbf{L}_p)^T\mathbf{m}^{i\prime}\,,$$

which can be used to show that the evolution equations for $({}_I\mathbf{s},{}_I\mathbf{n})$ in (9) can be expressed in the forms

$$\begin{aligned}{}_I\dot{\mathbf{s}} &= \big\{\mathbf{L}''-\mathbf{L}_p-\big[(\mathbf{L}''-\mathbf{L}_p)\cdot({}_I\mathbf{s}\otimes{}_I\mathbf{s})\big]\mathbf{I}\big\}{}_I\mathbf{s}\,,\\ {}_I\dot{\mathbf{n}} &= -\big\{\mathbf{L}''-\mathbf{L}_p-\big[(\mathbf{L}''-\mathbf{L}_p)\cdot({}_I\mathbf{n}\otimes{}_I\mathbf{n})\big]\mathbf{I}\big\}^T{}_I\mathbf{n}\,.\end{aligned} \tag{11}$$

2.1. Comparison with "classical" finite-deformation crystal plasticity relying on the multiplicative decomposition of the total deformation gradient

To clarify definition (7) of $\mathbf{L}_p$ in the current configuration and its relationship to the multiplicative representation $\mathbf{F}=\mathbf{F}_e\mathbf{F}_p$, the evolution equation for $\mathbf{F}_p$ used in (Rice, 1971; Asaro, 1983; Havner, 1992) can be expressed in the form

$$\dot{\mathbf{F}}_p = \boldsymbol{\Lambda}_p\mathbf{F}_p\,,\quad \boldsymbol{\Lambda}_p=\sum_{I=1}^{N}{}_I\Gamma^{\mathrm{ref}}\,{}_I\mathbf{S}\otimes{}_I\mathbf{N}\,,$$

where ${}_I\mathbf{N}$ is a unit vector normal to the Ith slip system, ${}_I\mathbf{S}$ is a unit vector in the slip plane in the direction of slip, and ${}_I\Gamma^{\mathrm{ref}}$ is the slip rate. In particular, ${}_I\mathbf{N},{}_I\mathbf{S}$ are specified as constant vectors in the intermediate configuration. These vectors are deformed into the current configuration by using the equations in (Asaro, 1983; Havner, 1992)

$${}_I\mathbf{s}^* = \mathbf{F}_e\,{}_I\mathbf{S}\,,\quad {}_I\mathbf{n}^* = \mathbf{F}_e^{-T}\,{}_I\mathbf{N}\,, \tag{12}$$

such that, in this classical formulation, the plastic rate has the form[2]

$$\mathbf{L}_p = \sum_{I=1}^{N}{}_I\Gamma^{\mathrm{ref}}\,{}_I\mathbf{s}^*\otimes{}_I\mathbf{n}^*\,,$$

which, with respect to (7), has the fundamental difference that, in general, the crystallographic directions ${}_I\mathbf{s}^*,{}_I\mathbf{n}^*$ are not unit vectors. Conceptually, this introduces a dependence on the choice of an intermediate configuration, which is not allowed in the adopted Eulerian formulation of constitutive equations, since the constitutive equations must depend only on internal state variables that are measurable in the current state. Also, a resolved shear stress, on the Ith slip system, computed by projecting the Cauchy stress onto ${}_I\mathbf{s}^*\otimes{}_I\mathbf{n}^*$ would be influenced by the stretches included in ${}_I\mathbf{s}^*,{}_I\mathbf{n}^*$. However, for metals the elastic stretches are nearly equal to unity.

A comparison between the two formulations in terms of kinematics is possible, as follows. From the equations

$$\dot{\mathbf{F}} = \mathbf{L}\mathbf{F}\,,\quad \dot{\overline{\mathbf{F}_p^{-1}}} = -\mathbf{F}_p^{-1}\boldsymbol{\Lambda}_p\,,$$

it can be shown that the evolution equation for elastic deformation in the classical formulation

$$\dot{\mathbf{F}}_e = (\mathbf{L}-\mathbf{L}_p)\mathbf{F}_e\,,\quad \mathbf{L}_p=\mathbf{F}_e\boldsymbol{\Lambda}_p\mathbf{F}_e^{-1}\,,$$

is consistent with the formulation (7) when

$${}_I\mathbf{s} = \frac{{}_I\mathbf{s}^*}{|{}_I\mathbf{s}^*|}\,,\quad {}_I\mathbf{n} = \frac{{}_I\mathbf{n}^*}{|{}_I\mathbf{n}^*|}\,,\quad {}_I\Gamma = |{}_I\mathbf{s}^*||{}_I\mathbf{n}^*|\,{}_I\Gamma^{\mathrm{ref}}\,, \tag{13}$$

where there is no sum on the repeated index I. Moreover, using these results and $\dot{\overline{\mathbf{F}_e^{-T}}} = -(\mathbf{L}-\mathbf{L}_p)^T\mathbf{F}_e^{-T}$, it can be shown that $({}_I\mathbf{s},{}_I\mathbf{n})$ in Eq. (13) also satisfy the evolution equations in (11) (note that those equations are not influenced by the spherical part $\mathrm{tr}(\mathbf{L})\mathbf{I}/3$ of $\mathbf{L}$). Hence, the crystallographic directions are identical for the two formulations, if in the classical formulation they are normalized as in Eq. (13). However, this correspondence would imply that the two formulations constitutively define different plastic slip rates, as specified by the third relation in Eq. (13).

2.2. Eulerian rates of elastic incompatibilities

Combining Eqs. (7) and (9) yields

$$\mathrm{curl}(\mathbf{L}_p) = -\Big(\sum_{I=1}^{N}{}_I\Gamma\,\frac{{}_Is^r\mathbf{m}_r'}{|{}_Is^q\mathbf{m}_q'|}\otimes\frac{{}_In_r\mathbf{m}^{r\prime}}{|{}_In_q\mathbf{m}^{q\prime}|}\Big)_{,k}\times\mathbf{g}^k\,, \tag{14}$$

where θ^i are arbitrary convected coordinates, such that

$$\mathbf{x}=\mathbf{x}(\theta^i,t)\,,\quad \mathbf{g}_i=\mathbf{x}_{,i}=\frac{\partial\mathbf{x}}{\partial\theta^i}\,,$$

in which the comma indicates partial differentiation with respect to θ^i and $\mathbf{g}_i$ $(i=1,2,3)$ is a triad of covariant base vectors in the current configuration, with contravariant base vectors $\mathbf{g}^i$ defined by

$$\begin{aligned}&\mathbf{g}^1=g^{-1/2}\mathbf{g}_2\times\mathbf{g}_3\,,\quad \mathbf{g}^2=g^{-1/2}\mathbf{g}_3\times\mathbf{g}_1\,,\quad \mathbf{g}^3=g^{-1/2}\mathbf{g}_1\times\mathbf{g}_2\,,\\ &g^{1/2}=\mathbf{g}_1\times\mathbf{g}_2\cdot\mathbf{g}_3>0\,,\quad \mathbf{g}_i\cdot\mathbf{g}^j=\delta_i^j\,,\quad \mathbf{g}_j\otimes\mathbf{g}^j=\mathbf{I}\,.\end{aligned} \tag{15}$$

Note that the covariant base vectors $\mathbf{G}_i=\mathbf{X}_{,i}=\partial\mathbf{X}/\partial\theta^i$ for the initial position $\mathbf{X}$ admit a contravariant base $\mathbf{G}^i$ defined as in Eq. (15) with $(g^{1/2},\mathbf{g}_i)$ substituted by $(G^{1/2},\mathbf{G}_i)$. This notation is useful to describe the Lagrangian kinematics, as in Section 4.1 for the bending problem.

By using Eq. (9), the transverse crystallographic direction, which is the direction belonging to the slip plane that is orthogonal to the slip direction, has the form

$${}_I\mathbf{t} = {}_I\mathbf{s}\times{}_I\mathbf{n} = \frac{1}{|{}_In_r\mathbf{m}^{r\prime}||{}_Is^q\mathbf{m}_q'|}[({}_Is^2\,{}_In_3-{}_Is^3\,{}_In_2)\mathbf{m}_1'$$

[2] Note that in several classical contributions in the literature on finite-deformation crystal plasticity, the symbol $\mathbf{L}_p$ is used for $\dot{\mathbf{F}}_p\mathbf{F}_p^{-1}$, while here the latter is denoted as $\boldsymbol{\Lambda}_p$.

$$+({}_I s^3\,{}_I n_1 - {}_I s^1\,{}_I n_3)\mathbf{m}'_2 + ({}_I s^1\,{}_I n_2 - {}_I s^2\,{}_I n_1)\mathbf{m}'_3]$$

and Eq. (14) can be rewritten as

$$\mathrm{curl}(\mathbf{L}_p) = -\sum_{I=1}^{N} {}_I\Gamma_{,k}\ {}_I\mathbf{s}\otimes({}_I\mathbf{t}\times{}_I\mathbf{s})\times\mathbf{g}^k - \sum_{I=1}^{N} {}_I\Gamma\left({}_I\mathbf{s}\otimes{}_I\mathbf{t}\times{}_I\mathbf{s}\right)_{,k}\times\mathbf{g}^k\,,$$

where the contribution involving the gradient of the plastic slip rates is the sole one non-vanishing under small strains and rotations. By using the triple product expansion $({}_I\mathbf{t}\times{}_I\mathbf{s})\times\mathbf{g}^k = {}_I\mathbf{s}({}_I\mathbf{t}\cdot\mathbf{g}^k) - {}_I\mathbf{t}({}_I\mathbf{s}\cdot\mathbf{g}^k)$, it follows that

$$\sum_{I=1}^{N} {}_I\Gamma_{,k}\,[-{}_I\mathbf{s}\otimes{}_I\mathbf{s}({}_I\mathbf{t}\cdot\mathbf{g}^k)+{}_I\mathbf{s}\otimes{}_I\mathbf{t}({}_I\mathbf{s}\cdot\mathbf{g}^k)] = \sum_{I=1}^{N}[{}_I\dot\rho_{\odot}\,{}_I\mathbf{s}\otimes{}_I\mathbf{s} + {}_I\dot\rho_{\perp}\,{}_I\mathbf{s}\otimes{}_I\mathbf{t}]\,,$$

where

$${}_I\dot\rho_{\odot} = -{}_I\Gamma_{,k}\,({}_I\mathbf{t}\cdot\mathbf{g}^k) \quad \text{and} \quad {}_I\dot\rho_{\perp} = {}_I\Gamma_{,k}\,({}_I\mathbf{s}\cdot\mathbf{g}^k)$$

represent rates of densities of pure screw and edge GNDs, respectively (Arsenlis and Parks, 1999). Therefore, Eq. (14) becomes

$$\mathrm{curl}(\mathbf{L}_p) = \sum_{I=1}^{N}({}_I\dot\rho_{\odot}\,{}_I\mathbf{s}\otimes{}_I\mathbf{s} + {}_I\dot\rho_{\perp}\,{}_I\mathbf{s}\otimes{}_I\mathbf{t}) - \sum_{I=1}^{N} {}_I\Gamma\left({}_I\mathbf{s}\otimes{}_I\mathbf{n}\right)_{,k}\times\mathbf{g}^k\,, \tag{16}$$

where

$$-\sum_{I=1}^{N} {}_I\Gamma\left({}_I\mathbf{s}\otimes{}_I\mathbf{n}\right)_{,k}\times\mathbf{g}^k = \sum_{I=1}^{N} {}_I\Gamma\,\mathrm{curl}({}_I\mathbf{s}\otimes{}_I\mathbf{n})$$

and

$$\begin{aligned}\mathrm{curl}({}_I\mathbf{s}\otimes{}_I\mathbf{n}) &= {}_I\mathbf{s}\otimes\mathrm{curl}({}_I\mathbf{n}) + ({}_I\mathbf{s}\otimes\nabla)\times{}_I\mathbf{n}\\ &= {}_I\mathbf{s}\otimes\mathrm{curl}({}_I\mathbf{n}) + ({}_I\mathbf{s}\otimes\nabla)\times({}_I\mathbf{t}\times{}_I\mathbf{s})\\ &= {}_I\mathbf{s}\otimes\mathrm{curl}({}_I\mathbf{n}) - [({}_I\mathbf{s}\otimes\nabla)_I\mathbf{t}]\otimes{}_I\mathbf{s} + [({}_I\mathbf{s}\otimes\nabla)_I\mathbf{s}]\otimes{}_I\mathbf{t}\\ &= {}_I\mathbf{s}\otimes\mathrm{curl}({}_I\mathbf{n}) + ({}_I\mathbf{s}\otimes\nabla)({}_I\mathbf{s}\otimes{}_I\mathbf{t} - {}_I\mathbf{t}\otimes{}_I\mathbf{s})\,,\end{aligned} \tag{17}$$

with the notation $\mathbf{s}\otimes\nabla \equiv \partial\mathbf{s}/\partial\mathbf{x}$.

The first contribution to $\mathrm{curl}(\mathbf{L}_p)$ in Eq. (16) is related to rates of GNDs, as in the plastically convected rate of the Nye-Kröner-like tensor developed by Gurtin (2006). However, Gurtin's rate differs from $\mathrm{curl}(\mathbf{L}_p)$ in Eq. (16) because in (Gurtin, 2006) the crystallographic directions are constants, whereas the second contribution to $\mathrm{curl}(\mathbf{L}_p)$ here depends on the elastic rotation of the orthonormal crystal lattice vectors $\mathbf{s}_I$ and $\mathbf{n}_I$.

So, one of the central results of this investigation is attained by combining Eqs. (3) and (16) to obtain the expressions

$$\begin{aligned}&R_{ij} = R_{ij}^{\mathrm{GND}} + R_{ij}^{\mathrm{ed}}\,,\\ &R_{ij}^{\mathrm{GND}} = -\left\{\sum_{I=1}^{N}[{}_I\dot\rho_{\odot}\,{}_I\mathbf{s}\otimes{}_I\mathbf{s} + {}_I\dot\rho_{\perp}\,{}_I\mathbf{s}\otimes{}_I\mathbf{t}]\right\}\cdot(\mathbf{m}'_i\otimes\mathbf{m}'_j)\\ &R_{ij}^{\mathrm{ed}} = \left[\sum_{I=1}^{N} {}_I\Gamma\,\mathrm{curl}({}_I\mathbf{s}\otimes{}_I\mathbf{n})\right]\cdot(\mathbf{m}'_i\otimes\mathbf{m}'_j)\\ &\quad = \left\{\sum_{I=1}^{N} {}_I\Gamma[{}_I\mathbf{s}\otimes\mathrm{curl}({}_I\mathbf{n}) + ({}_I\mathbf{s}\otimes\nabla)({}_I\mathbf{s}\otimes{}_I\mathbf{t} - {}_I\mathbf{t}\otimes{}_I\mathbf{s})]\right\}\cdot(\mathbf{m}'_i\otimes\mathbf{m}'_j)\,,\end{aligned} \tag{18}$$

where R_{ij}^{GND} and R_{ij}^{ed} are the contributions to the rates of elastic incompatibilities due, respectively, to rates of GNDs densities and to the distortion of the crystal lattice.

One of the objectives of this study is the evaluation of the importance in the modeling of the contribution R_{ij}^{ed} in Eq. (18).

3. A crystal plasticity constitutive theory including elastic incompatibilities

A purely mechanical theory is considered for which the rate of material dissipation D has the form

$$D = \mathbf{T}\cdot\mathbf{D} - \rho\dot\Sigma \geq 0\,, \tag{19}$$

where ρ is the current mass density,

$$\mathbf{D} = \frac{1}{2}(\mathbf{L}+\mathbf{L}^T)$$

is the total deformation rate, and Σ is the Helmholtz free energy per unit mass.

3.1. General anisotropic elastoplastic response

In this case, the free energy is assumed to have the form

$$\Sigma = \Sigma(J_e, m'_{ij})\,, \tag{20}$$

where m'_{ij} is the elastic distortional deformation metric, defined as

$$m'_{ij} = \mathbf{m}'_i\cdot\mathbf{m}'_j \tag{21}$$

and satisfying

$$\dot m'_{ij} = 2(\mathbf{m}'_i\otimes\mathbf{m}'_j - \frac{m'_{ij}}{3}\mathbf{I})\cdot(\mathbf{D}-\mathbf{D}_p)\,. \tag{22}$$

Also, since the material derivative of Eq. (4) yields

$$\frac{\dot J_e}{J_e} = \dot{\mathbf{m}}_j\cdot\mathbf{m}^j = \mathrm{tr}(\mathbf{L}-\mathbf{L}_p) = \mathrm{tr}(\mathbf{D})\,, \tag{23}$$

the elastic dilatation in Eq. (4) can then be rewritten, by using the conservation of mass and Eq. (23), as

$$J_e = \frac{\rho_z}{\rho}\,, \tag{24}$$

where ρ_z is the constant value of the mass density in the RLS.

Next, Eqs. (20)–(23) allow the Cauchy stress to be defined as

$$\mathbf{T} = -p\mathbf{I} + \mathbf{T}''\,, \quad p = -\rho J_e\frac{\partial\Sigma}{\partial J_e}\,, \quad \mathbf{T}'' = 2\rho\frac{\partial\Sigma}{\partial m'_{ij}}(\mathbf{m}'_i\otimes\mathbf{m}'_j - \frac{m'_{ij}}{3}\mathbf{I}) \tag{25}$$

and, by using Eq. (8), the rate of material dissipation (19) requires

$$\mathcal{D} = \mathbf{T}''\cdot\mathbf{D}_p = \sum_{I=1}^{N}\frac{{}_I\Gamma}{2}({}_I\mathbf{s}\otimes{}_I\mathbf{n} + {}_I\mathbf{n}\otimes{}_I\mathbf{s})\cdot\mathbf{T}'' = \sum_{I=1}^{N} {}_I\Gamma\,{}_I\tau \geq 0\,, \tag{26}$$

where

$${}_I\tau = \mathbf{T}''\cdot({}_I\mathbf{s}\otimes{}_I\mathbf{n}) \tag{27}$$

is the resolved shear stress, also denoted as the Schmid stress, acting on the Ith slip system.

Moreover, the free energy is restricted so that in a RLS $J_e = 1$ and $m'_{ij} = \delta_{ij}$, the latter being the Kronecker delta.

3.2. Elastoplastic response with isotropic elasticity

By assuming elastically isotropic response, the symmetric elastic distortional deformation $\mathbf{B}'_e$ can be defined as

$$\mathbf{B}'_e = \mathbf{m}'_k\otimes\mathbf{m}'_k\,, \quad \mathbf{B}'^{-1}_e = \mathbf{m}^{k\prime}\otimes\mathbf{m}^{k\prime}\,. \tag{28}$$

By using the evolution equation in (1) and the plastic rate in Eq. (7), the time derivative of (28) yields

$$\begin{aligned}\dot{\mathbf{B}}'_e &= \mathbf{L}''\mathbf{B}'_e + \mathbf{B}'_e\mathbf{L}''^T - (\mathbf{L}_p\mathbf{B}'_e + \mathbf{B}'_e\mathbf{L}_p^T)\\ &= \mathbf{L}''\mathbf{B}'_e + \mathbf{B}'_e\mathbf{L}''^T - \sum_{I=1}^{N} {}_I\Gamma\left[{}_I\mathbf{s}\otimes({}_I\mathbf{B}'_e\,{}_I\mathbf{n}) + ({}_I\mathbf{B}'_e\,{}_I\mathbf{n})\otimes{}_I\mathbf{s}\right],\end{aligned} \tag{29}$$

which ensures that $\mathbf{B}'_e$ remains unimodular (i.e. $\dot{\mathbf{B}}'_e\cdot\mathbf{B}'^{-1}_e = 0$). Noticeably, in the absence of plasticity the evolution equation in (29) ensures that $\mathbf{B}'_e$ is the unimodular part $\mathbf{B}'$ of the left Cauchy–Green deformation tensor all along the loading history if $\mathbf{B}'_e = \mathbf{B}'$ in any instant.

Within isotropic elasticity for metals, the free energy can be selected as

$$\rho_z\Sigma = k\left[J_e - 1 - \ln(J_e)\right] + \frac{1}{2}\mu[\mathrm{tr}(\mathbf{B}'_e) - 3]\,,$$

where k and μ are the zero-stress bulk and shear moduli. Then, by substituting Eqs. (24) and (28) in Eq. (25), the Cauchy stress becomes

$$p = k\Big(\frac{1}{J_e} - 1\Big), \quad \mathbf{T}'' = J_e^{-1}\mu\mathbf{B}_e''. \tag{30}$$

Therefore, the Schmid stress in (27) can be written in the form

$${}_I\tau = J_e^{-1}\mu\,{}_I\gamma_e, \quad {}_I\gamma_e = \mathbf{B}_e'' \cdot ({}_I\mathbf{s} \otimes {}_I\mathbf{n}), \tag{31}$$

where ${}_I\gamma_e$ is the elastic engineering shear strain driving plasticity in the Ith slip system.

3.3. A smooth elastoplastic transition with length-dependent hardening

Each plastic slip rate ${}_I\Gamma$ in Eq. (7) is typically a function of history-dependent variables. Incorporating a smooth elastoplastic transition (Hollenstein et al., 2013, 2015) has the advantage of avoiding non-uniqueness in the activation of slip systems that is typical of rate-independent crystal plasticity based on conventional consistency conditions (Gambin, 1992; Forest and Rubin, 2016).

A simple form of the smooth elastoplastic transition model for rate-independent crystal plasticity can be proposed, for each slip system, in the form

$${}_I\Gamma = {}_Ib\,{}_I\dot\gamma\,\langle {}_Ig\rangle\frac{{}_I\gamma_e}{|{}_I\gamma_e|}, \quad {}_I\dot\gamma = |\mathbf{D}'' \cdot ({}_I\mathbf{s} \otimes {}_I\mathbf{n})|, \quad {}_Ig = |{}_I\gamma_e| - {}_IY, \tag{32}$$

where ${}_Ib > 0$ is a material parameter, ${}_I\dot\gamma$ is the total engineering shear strain rate acting on the Ith slip system, ${}_Ig$ is a yield function, ${}_IY > 0$ is a strain-type hardening variable, and

$$\langle x\rangle = \max(x, 0)$$

are the Macaulay brackets.

The response predicted by the model (32) features a smooth elastoplastic transition with overstress on each slip system. Increasing ${}_Ib$ leads to a sharper transition and a smaller overstress. Also, the definition of ${}_I\Gamma$ in Eq. (32) allows the dissipation inequality (26) to be automatically satisfied.

3.3.1. Isotropic hardening, including size-dependence with latent hardening

The invariance of R_{ij} under SRBM allows any appropriate function of the R_{ij} components to be selected as a field to extend the hardening to include size-dependence in the model. The present work follows the proposal in (Rubin and Bardella, 2024) for phenomenological plasticity, thus considering the scalar field ξ defined by the sum of all the R_{ij} components. This is the simplest combination of the R_{ij} components that allows ξ to increase due to generation of defects and to decrease due to annihilation of defects. Accounting for the two contributions identified in Eq. (18) yields

$$\begin{aligned}
&\dot\xi = \dot\xi^{\mathrm{GND}} + \dot\xi^{\mathrm{ed}},\\
&\dot\xi^{\mathrm{GND}} = \ell\sum_{i=1}^{3}\sum_{j=1}^{3} R_{ij}^{\mathrm{GND}}\\
&\qquad = -\ell\sum_{i=1}^{3}\sum_{j=1}^{3}\left\{\sum_{I=1}^{N}[{}_I\dot\rho_{\odot}\,{}_I\mathbf{s}\otimes{}_I\mathbf{s} + {}_I\dot\rho_{\perp}\,{}_I\mathbf{s}\otimes{}_I\mathbf{t}]\right\}\cdot(\mathbf{m}_i'\otimes\mathbf{m}_j'),\\
&\dot\xi^{\mathrm{ed}} = \ell\sum_{i=1}^{3}\sum_{j=1}^{3} R_{ij}^{\mathrm{ed}} = \ell\sum_{i=1}^{3}\sum_{j=1}^{3}\left[\sum_{I=1}^{N}{}_I\Gamma\,\mathrm{curl}({}_I\mathbf{s}\otimes{}_I\mathbf{n})\right]\cdot(\mathbf{m}_i'\otimes\mathbf{m}_j'),
\end{aligned} \tag{33}$$

where $\dot\xi^{\mathrm{GND}}$ and $\dot\xi^{\mathrm{ed}}$ are the contributions due to GNDs densities and distortion of the crystal lattice, respectively, and $\ell \geq 0$ is a characteristic material length.

The field ξ enhances, for each Ith slip system, a history-dependent hardening parameter ${}_IY$ having the form

$$\begin{aligned}
&{}_IY = {}_IY_H + {}_IY_\ell, \quad {}_I\dot Y_H = |{}_I\Gamma|\,{}_Im_H({}_IY_{Hs} - {}_IY_H),\\
&{}_I\dot Y_\ell = |\dot\xi|\big[{}_Im_\ell\langle {}_IY_R - {}_IY_\ell\rangle - {}_Im_r\langle {}_IY_\ell - {}_IY_R\rangle\big],\\
&{}_IY_R = {}_IY_{Rs}\,(1 - 10^{-|\xi|})^{{}_In_R},
\end{aligned} \tag{34}$$

which is controlled by the eight non-negative material parameters ${}_IY_{H0}$, ${}_Im_H$, ${}_IY_{Hs}$, ${}_IY_R$, ${}_IY_{Rs}$, ${}_Im_\ell$, ${}_Im_r$, and ${}_In_R$. Specifically, ${}_IY_{H0}$ sets the initial yield point in the Ith slip system through the annealed conditions

$${}_IY_H(t=0) = {}_IY_{H0}, \quad {}_IY_\ell(t=0) = 0 \;\forall I, \tag{35}$$

${}_Im_H$ governs the rate of monotonic increase of the conventional hardening ${}_IY_H$, from its initial value ${}_IY_{H0}$ up to the saturated value ${}_IY_{Hs}$. The size-dependent hardening ${}_IY_\ell$ can instead increase or decrease between 0 and its saturated value ${}_IY_R$ that depends on $|\xi|$ and admits the maximum value ${}_IY_{Rs}$, the latter being set by the last relation in Eq. (34) where ${}_In_R$ governs the profile of the function ${}_IY_R(|\xi|)$, thus establishing the number of orders of magnitude of size showing appreciable size-effect. Finally, ${}_Im_\ell$ and ${}_Im_r$ control, respectively, the rates of increase and decrease of ${}_IY_\ell$, the decrease being ascribed to annihilation of defects. Note that for ${}_Im_r = {}_Im_\ell$ the third relation in Eq. (34) simply becomes ${}_I\dot Y_\ell = |\dot\xi|\,{}_Im_\ell({}_IY_R - {}_IY_\ell)$.

For the present case of crystal plasticity, as is clear from the coupling among slip systems in Eq. (33), the definitions (33) and (34) introduce some lower-order size-dependent latent hardening in the model. A complex form of this kind of contribution was proposed in Bardella et al. (2013) to supplement a higher-order theory of strain gradient crystal plasticity (Bardella, 2006; Gurtin et al., 2007) to predict the results of discrete dislocation dynamics simulations.

It is worth remarking that in the models proposed here and in (Rubin and Bardella, 2024) the onset of yielding is size-independent. This notwithstanding, the adopted smooth elastoplastic transition in Eq. (32) allows for the prediction of an increase of the *apparent* yield stress with diminishing size (i.e. strengthening) because the rate of plasticity is zero at the onset of yielding. In other words, in this modeling the size-dependent hardening begins to influence the material behavior before plasticity can be recognized in the stress–strain curve, which is also the goal of more complex higher-order SGP theories (Rubin and Bardella, 2023; Amouzou-Adoun et al., 2024; Panteghini et al., 2025) recently developed, by following the remarks of Fleck et al. (2014), to avoid the drawbacks of "non-incremental" SGP theories along with other issues (Panteghini et al., 2019).

The present framework could be modified to develop an Eulerian higher-order strain gradient crystal plasticity by following Rubin and Bardella (2023). This would require the determination of $\boldsymbol{\alpha}_e$ by time-integrating a Jaumann derivative suitably modifying the right-hand side of Eq. (2). Then, $\boldsymbol{\alpha}_e$ could be constitutively associated to a higher-order stress by adding to the Helmholtz free-energy density a contribution dependent on $\boldsymbol{\alpha}_e$, which is usually referred to as the defect energy (Gurtin, 2000). The higher-order stress would enter a higher-order balance equation with related higher-order boundary conditions, the latter allowing the modeling of dislocations' pile-ups at hard boundaries and interfaces (Gurtin and Needleman, 2005), resulting into a size-dependent Bauschinger effect (see, e.g., Panteghini and Bardella, 2020).

4. Finite cyclic bending

This benchmark problem follows the work in (Green and Zerna, 1954) and, as depicted in Fig. 1, considers uniform bending of a sector of right circular cylinder that in its RLS has inner radius A, outer radius B, thickness

$$H = B - A, \tag{36}$$

and axial length L. Moreover, the material is assumed to be elastically isotropic, homogeneous, and incompressible, with the pressure being a field that is determined by the balance of linear momentum and boundary conditions. The cylindrical sector is subjected to uniform bending encompassing loading and reverse loading.

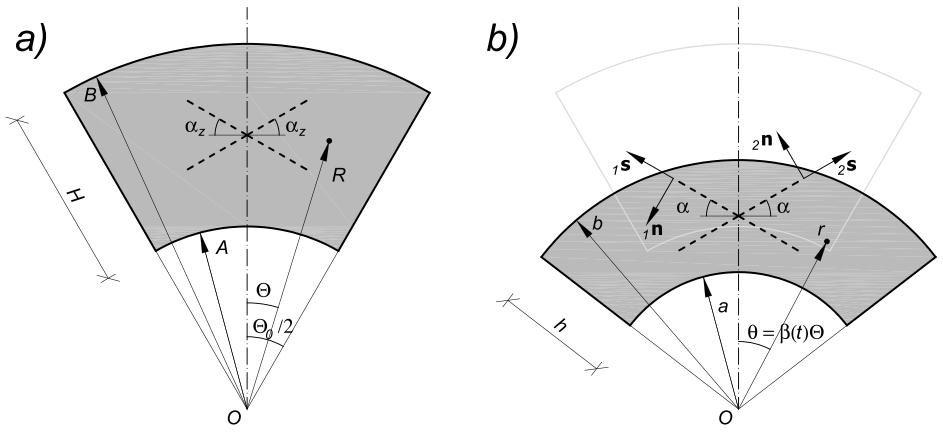

Fig. 1. Uniform isochoric bending of a sector of right circular cylinder: undeformed configuration (a) and current configuration (b).

4.1. Lagrangian kinematics

It is emphasized that, although the constitutive equations must be formulated in terms of Eulerian internal state variables, the resulting equations can be solved by adopting Lagrangian or Eulerian formulations. Using cylindrical base vectors, the position vector $\hat{\mathbf{X}}$ of a material point is given by

$$\hat{\mathbf{X}} = R\mathbf{e}_r(\Theta) + Z\mathbf{e}_z\,,$$

and the boundaries of the shell's sector are defined by (see Fig. 1a)

$$A \le R \le B = A + H\,, \quad -\frac{\Theta_0}{2} \le \Theta \le \frac{\Theta_0}{2}\,, \quad 0 \le Z \le L\,. \tag{37}$$

$\Theta_0 > 0$ defines the arc of the shell's sector and it is introduced only for completeness, as it is irrelevant in stress and deformation states under uniform bending. The associated covariant $\hat{\mathbf{G}}_i$ base vectors are given by

$$\hat{\mathbf{G}}_1 = \frac{\partial\hat{\mathbf{X}}}{\partial R} = \mathbf{e}_r\,, \quad \hat{\mathbf{G}}_2 = \frac{\partial\hat{\mathbf{X}}}{\partial\Theta} = R\mathbf{e}_\theta(\Theta)\,, \quad \hat{\mathbf{G}}_3 = \frac{\partial\hat{\mathbf{X}}}{\partial Z} = \mathbf{e}_z\,,$$
$$\hat{G}^{1/2} = \hat{\mathbf{G}}_1 \times \hat{\mathbf{G}}_2 \cdot \hat{\mathbf{G}}_3 = R\,,$$

The location $\mathbf{x}$ of a material point in the current configuration is expressed in the form

$$\mathbf{x} = r\mathbf{e}_r(\theta) + z\mathbf{e}_z\,, \tag{38}$$

with the specifications

$$r = r(R,t) > 0\,, \quad \theta = \beta(t)\Theta\,, \quad z = \lambda(t)Z\,, \tag{39}$$

where $\beta(t) > 0$ is a structural stretch along the circumferential direction (see Fig. 1b) and $\lambda(t) > 0$ is a uniform axial stretch along the direction Z, i.e. normal to the bending plane, so the solid sections normal to Z remain planar upon deformation, belonging to a plane parallel to $Z = 0$. Note that plane-strain bending is obtained by imposing $\lambda = 1\ \forall t$. The kinematics imposed by the third relation in Eq. (39) makes the length L in Eq. (37) irrelevant for the stress and deformation states. Also, the independence of r on θ in Eq. (39) holds in the absence of shear force on the cross-sections of normal $\pm\mathbf{e}_\theta$, which, under the kinematics in Eq. (39), is obvious in the elastic case, while in the plastic regime it holds only under specific assumptions on the crystallography.

In the reference configuration, i.e. at $t = 0$,

$$r(R,0) = R\,, \quad \beta(0) = 1\,, \quad \lambda(0) = 1\,. \tag{40}$$

The covariant base vectors $\tilde{\mathbf{g}}_i$ in the current configuration are given by

$$\tilde{\mathbf{g}}_1 = \frac{\partial\mathbf{x}}{\partial R} = \frac{\partial r}{\partial R}\mathbf{e}_r(\theta)\,, \quad \tilde{\mathbf{g}}_2 = \frac{\partial\mathbf{x}}{\partial\Theta} = r\beta\mathbf{e}_\theta(\theta)\,, \quad \tilde{\mathbf{g}}_3 = \frac{\partial\mathbf{x}}{\partial Z} = \lambda\mathbf{e}_z\,,$$
$$\tilde{g}^{1/2} = \tilde{\mathbf{g}}_1 \times \tilde{\mathbf{g}}_2 \cdot \tilde{\mathbf{g}}_3 = r\lambda\beta\frac{\partial r}{\partial R}\,. \tag{41}$$

For isochoric deformation, the total dilatation satisfies the restriction

$$\frac{\tilde{g}^{1/2}}{\hat{G}^{1/2}} = \frac{r\lambda\beta}{R}\frac{\partial r}{\partial R} = 1\,, \tag{42}$$

which can be integrated to deduce that

$$r^2 = a(t)^2 + \frac{R^2 - A^2}{\lambda\beta}\,, \quad \frac{\partial r}{\partial R} = \frac{R}{r\lambda\beta}\,, \tag{43}$$

where $a(t)$ is the inner radius in the current configuration, i.e. $a(0) = R(A,0) = A$. It follows that the outer radius $b(t)$ of the deformed sector, with $b(0) = R(B,0) = B$, is given by

$$b(t)^2 = a(t)^2 + \frac{B^2 - A^2}{\lambda\beta}\,, \tag{44}$$

which can be seen as a constraint due to the assumed isochoric deformation.

The current thickness, as displayed in Fig. 1b, is denoted as

$$h(t) = b(t) - a(t)\,, \quad \text{such that} \quad h(0) = H\,. \tag{45}$$

4.2. Eulerian kinematics

In the Eulerian formulation the position vector $\mathbf{x}$ is given by Eq. (38) and the covariant $\mathbf{g}_i$ and contravariant $\mathbf{g}^i$ base vectors are given by

$$\mathbf{g}_1 = \frac{\partial\mathbf{x}}{\partial r}\mathbf{e}_r\,, \quad \mathbf{g}_2 = \frac{\partial\mathbf{x}}{\partial\theta} = r\mathbf{e}_\theta\,, \quad \mathbf{g}_3 = \frac{\partial\mathbf{x}}{\partial z} = \mathbf{e}_z\,,$$
$$g^{1/2} = \mathbf{g}_1 \times \mathbf{e}_2 \cdot \mathbf{g}_3 = r > 0\,, \quad \mathbf{g}^1 = g^{-1/2}\mathbf{g}_2 \times \mathbf{g}_3 = \mathbf{e}_r\,, \tag{46}$$
$$\mathbf{g}^2 = g^{-1/2}\mathbf{g}_3 \times \mathbf{g}_1 = \frac{1}{r}\mathbf{e}_\theta\,, \quad \mathbf{g}^3 = g^{-1/2}\mathbf{g}_1 \times \mathbf{g}_2 = \mathbf{e}_z\,.$$

An evolution equation for r is obtained by taking the material derivative of Eq. (43) and writing the result in the form

$$\frac{\dot r}{r} = \frac{a\dot a}{r^2} - \frac{1}{2}\left(1 - \frac{a^2}{r^2}\right)\left(\frac{\dot\beta}{\beta} + \frac{\dot\lambda}{\lambda}\right). \tag{47}$$

Also, an evolution equation for b can be obtained by setting $r = b$ in Eq. (47) to find

$$\frac{\dot b}{b} = \frac{a\dot a}{b^2} - \frac{1}{2}\left(1 - \frac{a^2}{b^2}\right)\left(\frac{\dot\beta}{\beta} + \frac{\dot\lambda}{\lambda}\right), \tag{48}$$

which is the same as taking the material derivative of Eq. (44). Then, from taking the material time derivative of the second and third relations in Eq. (39), it follows that

$$\dot\theta = \frac{\dot\beta}{\beta}\theta\,, \quad \dot z = \frac{\dot\lambda}{\lambda}z\,. \tag{49}$$

Hence, by using Eq. (38), the velocity is given by

$$\mathbf{v} = v_r\mathbf{e}_r + v_\theta\mathbf{e}_\theta + v_z\mathbf{e}_z\,, \quad v_r = \dot r\,, \quad v_\theta = \frac{\dot\beta}{\beta}\theta r\,, \quad v_z = \frac{\dot\lambda}{\lambda}z\,, \tag{50}$$

where, with the help of Eq. (47), the radial velocity can also be written as

$$v_r = \frac{a\dot{a}}{r} - \frac{1}{2}\left(r - \frac{a^2}{r}\right)\left(\frac{\dot{\beta}}{\beta} + \frac{\dot{\lambda}}{\lambda}\right). \tag{51}$$

Next, the velocity gradient $\mathbf{L}$, which is given by

$$\mathbf{L} = \frac{\partial \mathbf{v}}{\partial r} \otimes \mathbf{g}^1 + \frac{\partial \mathbf{v}}{\partial \theta} \otimes \mathbf{g}^2 + \frac{\partial \mathbf{v}}{\partial z} \otimes \mathbf{g}^3,$$

can be written, using Eqs. (46) and (50), as

$$\begin{aligned}\mathbf{L} &= \left(\frac{\partial v_r}{\partial r}\mathbf{e}_r + \frac{\partial v_\theta}{\partial r}\mathbf{e}_\theta\right) \otimes \mathbf{e}_r + \left(v_r\mathbf{e}_\theta + \frac{\partial v_\theta}{\partial \theta}\mathbf{e}_\theta - v_\theta\mathbf{e}_r\right) \otimes \frac{1}{r}\mathbf{e}_\theta + \frac{\partial v_z}{\partial z}\mathbf{e}_z \otimes \mathbf{e}_z \\ &= \frac{\partial v_r}{\partial r}\mathbf{e}_r \otimes \mathbf{e}_r + \frac{1}{r}\left(v_r + \frac{\dot{\beta}}{\beta}r\right)\mathbf{e}_\theta \otimes \mathbf{e}_\theta + \frac{\dot{\lambda}}{\lambda}\mathbf{e}_z \otimes \mathbf{e}_z \\ &\quad -\frac{\dot{\beta}}{\beta}\theta\mathbf{e}_r \otimes \mathbf{e}_\theta + \frac{\dot{\beta}}{\beta}\theta\mathbf{e}_\theta \otimes \mathbf{e}_r.\end{aligned} \tag{52}$$

Since the deformation is isochoric

$$\mathbf{L}\cdot\mathbf{I} = \frac{\partial v_r}{\partial r} + \frac{1}{r}\left(v_r + \frac{\partial v_\theta}{\partial \theta}\right) + \frac{\dot{\lambda}}{\lambda} = 0 \tag{53}$$

and, by using the second and third relations in Eq. (50), it can be shown that

$$\frac{1}{r}\left(v_r + \frac{\partial v_\theta}{\partial \theta}\right) = \frac{\dot{r}}{r} + \frac{\dot{\beta}}{\beta}. \tag{54}$$

Therefore, by combining Eqs. (53) and (54), it follows that

$$\frac{\partial v_r}{\partial r} = -\left(\frac{\dot{r}}{r} + \frac{\dot{\beta}}{\beta} + \frac{\dot{\lambda}}{\lambda}\right), \tag{55}$$

which can be verified by comparing the derivative with respect to r of Eq. (51) with the right-hand-side of Eq. (55) combined with Eq. (47).

Thus, from Eq. (52), the deviatoric parts of the total velocity gradient and total deformation rate become

$$\begin{aligned}\mathbf{L}'' &= -\left(\frac{\dot{r}}{r} + \frac{\dot{\beta}}{\beta} + \frac{\dot{\lambda}}{\lambda}\right)\mathbf{e}_r \otimes \mathbf{e}_r + \left(\frac{\dot{r}}{r} + \frac{\dot{\beta}}{\beta}\right)\mathbf{e}_\theta \otimes \mathbf{e}_\theta + \frac{\dot{\lambda}}{\lambda}\mathbf{e}_z \otimes \mathbf{e}_z \\ &\quad + \theta\frac{\dot{\beta}}{\beta}(-\mathbf{e}_r \otimes \mathbf{e}_\theta + \mathbf{e}_\theta \otimes \mathbf{e}_r), \\ \mathbf{D}'' &= -\left(\frac{\dot{r}}{r} + \frac{\dot{\beta}}{\beta} + \frac{\dot{\lambda}}{\lambda}\right)\mathbf{e}_r \otimes \mathbf{e}_r + \left(\frac{\dot{r}}{r} + \frac{\dot{\beta}}{\beta}\right)\mathbf{e}_\theta \otimes \mathbf{e}_\theta + \frac{\dot{\lambda}}{\lambda}\mathbf{e}_z \otimes \mathbf{e}_z.\end{aligned} \tag{56}$$

4.3. Elastic response

Because of the symmetries of the bending problem, the microstructural vectors $\mathbf{m}'_i$ are specified by

$$\begin{aligned}&\mathbf{m}'_1 = m'_{1r}\mathbf{e}_r, \quad \mathbf{m}'_2 = m'_{2\theta}\mathbf{e}_\theta, \quad \mathbf{m}'_3 = m'_{3z}\mathbf{e}_z, \quad m'_{3z} = \frac{1}{m'_{1r}m'_{2\theta}}, \\ &\mathbf{m}^{1\prime} = \frac{1}{m'_{1r}}\mathbf{e}_r, \quad \mathbf{m}^{2\prime} = \frac{1}{m'_{2\theta}}\mathbf{e}_\theta, \quad \mathbf{m}^{3\prime} = m'_{1r}m'_{2\theta}\mathbf{e}_z,\end{aligned} \tag{57}$$

which, with the help of Eq. (49), yields

$$\begin{aligned}\dot{\mathbf{m}}'_1 &= \dot{m}'_{1r}\mathbf{e}_r + \frac{\dot{\beta}}{\beta}\theta m'_{1r}\mathbf{e}_\theta, \\ \dot{\mathbf{m}}'_2 &= \dot{m}'_{2\theta}\mathbf{e}_\theta - \frac{\dot{\beta}}{\beta}\theta m'_{2\theta}\mathbf{e}_r, \\ \dot{\mathbf{m}}'_3 &= \dot{m}'_{3z}\mathbf{e}_z.\end{aligned} \tag{58}$$

Moreover, combining the first three relations in Eq. (57) with the first relation in Eq. (56) yields

$$\begin{aligned}\mathbf{L}''\mathbf{m}'_1 &= -\left(\frac{\dot{r}}{r} + \frac{\dot{\beta}}{\beta} + \frac{\dot{\lambda}}{\lambda}\right)m'_{1r}\mathbf{e}_r + \theta\frac{\dot{\beta}}{\beta}m'_{1r}\mathbf{e}_\theta, \\ \mathbf{L}''\mathbf{m}'_2 &= \left(\frac{\dot{r}}{r} + \frac{\dot{\beta}}{\beta}\right)m'_{2\theta}\mathbf{e}_\theta - \theta\frac{\dot{\beta}}{\beta}m'_{2\theta}\mathbf{e}_r, \\ \mathbf{L}''\mathbf{m}'_3 &= \frac{\dot{\lambda}}{\lambda}\dot{m}'_{3z}\mathbf{e}_z.\end{aligned} \tag{59}$$

For elastic response, setting $\mathbf{L}_p = \mathbf{0}$ in the evolution Eq. (5) for $\mathbf{m}'_i$, along with comparison of Eqs. (58) and (59), leads to

$$\begin{aligned}\dot{m}'_{1r} &= -\left(\frac{\dot{r}}{r} + \frac{\dot{\beta}}{\beta} + \frac{\dot{\lambda}}{\lambda}\right)m'_{1r}, \\ \dot{m}'_{2\theta} &= \left(\frac{\dot{r}}{r} + \frac{\dot{\beta}}{\beta}\right)m'_{2\theta}, \\ \dot{m}'_{3z} &= \frac{\dot{\lambda}}{\lambda}m'_{3z},\end{aligned} \tag{60}$$

which can be solved to obtain

$$\mathbf{m}'_1 = \frac{R}{r\lambda\beta}\mathbf{e}_r, \quad \mathbf{m}'_2 = \frac{r\beta}{R}\mathbf{e}_\theta, \quad \mathbf{m}'_3 = \lambda\mathbf{e}_z, \tag{61}$$

where use has been made of the initial conditions in Eq. (40) along with $m'_{1r}(t=0) = 1$, $m'_{2\theta}(t=0) = 1$, and $m'_{3z}(t=0) = 1$.

As in Eq. (30), the deviatoric part of the Cauchy stress $\mathbf{T}''$ is proportional through the shear modulus μ to $\mathbf{B}''_e$, the latter following from Eqs. (28) and (61). This leads to

$$\begin{aligned}\mathbf{T}'' = \frac{\mu}{3}\Bigg\{ &\left[2\left(\frac{R}{r\lambda\beta}\right)^2 - \left(\frac{r\beta}{R}\right)^2 - \lambda^2\right]\mathbf{e}_r \otimes \mathbf{e}_r \\ &+ \left[-\left(\frac{R}{r\lambda\beta}\right)^2 + 2\left(\frac{r\beta}{R}\right)^2 - \lambda^2\right]\mathbf{e}_\theta \otimes \mathbf{e}_\theta \\ &+ \left[-\left(\frac{R}{r\lambda\beta}\right)^2 - \left(\frac{r\beta}{R}\right)^2 + 2\lambda^2\right]\mathbf{e}_z \otimes \mathbf{e}_z\Bigg\}.\end{aligned} \tag{62}$$

Given the absence of body forces, the sole non-trivial balance equation reads

$$\frac{\partial(rT_{rr})}{\partial r} - T_{\theta\theta} = T''_{rr} + r\frac{\partial(T''_{rr} - p)}{\partial r} - T''_{\theta\theta} = 0, \tag{63}$$

such as

$$\frac{\partial T_{rr}}{\partial r} = \frac{T''_{\theta\theta} - T''_{rr}}{r} = \frac{\mu}{r}\left[-\left(\frac{R}{r\lambda\beta}\right)^2 + \left(\frac{r\beta}{R}\right)^2\right], \tag{64}$$

whose integration under the conditions

$$T_{rr}(a,t) = 0 \quad \text{and} \quad T_{rr}(b,t) = 0 \tag{65}$$

allows the determination of an integration constant and a nonlinear algebraic equation providing β as a function of a for a given λ, the latter reading

$$\frac{1}{\lambda\beta}\left(\frac{A^2}{a^2} - \frac{B^2}{b^2}\right) + \ln\frac{b^2}{a^2} = \beta^2\ln\frac{B^2}{A^2}, \tag{66}$$

where the outer radius b is given in terms of a by Eq. (44).

Notably, determining $\lambda\beta$ from Eq. (44), substituting it into Eq. (66), and using Eq. (45) yields

$$\frac{(h/a)^2 + 2h/a}{B^2 - A^2}\left[A^2 - \frac{B^2}{(1+h/a)^2}\right] + \ln\left(1 + \frac{h}{a}\right)^2 = \beta^2\ln\frac{B^2}{A^2}, \tag{67}$$

which shows that the ratio h/a is independent of λ, so, for a given β its value is unaffected by the imposed out-of-plane condition (either plane strain or prescribed axial force along the z direction). Hence, by resorting to the terminology of structural mechanics, the shell *thickness* (relative to a) depends on the behavior in the r,θ plane only.

By using, $p = T''_{rr} - T_{rr} = T''_{\theta\theta} - T_{\theta\theta}$, after some lengthy algebra, the radial and circumferential normal stresses and the pressure can be expressed in the forms

$$\begin{aligned}T_{rr} &= \frac{\mu}{2\lambda\beta}\left\{1 - \frac{a^2}{r^2} + \frac{A^2}{\lambda\beta}\left(\frac{1}{r^2} - \frac{1}{a^2}\right) - \ln\frac{r^2}{a^2} + \beta^2\ln\left[1 + \frac{\lambda\beta}{A^2}(r^2 - a^2)\right]\right\}, \\ T_{\theta\theta} &= \frac{\mu}{2\lambda\beta}\Bigg\{-\frac{1}{r^2}\left(r^2 - a^2\right) - \frac{A^2}{\lambda\beta}\left(\frac{1}{a^2} + \frac{1}{r^2}\right) \\ &\quad + \beta^2\ln\left(1 + \lambda\beta\frac{r^2 - a^2}{A^2}\right) - \ln\frac{r^2}{a^2} + 2\lambda\beta\left[\frac{\lambda}{\beta}\left(1 - \frac{a^2}{r^2}\right) + \frac{A^2}{(r\beta)^2}\right]^{-1}\Bigg\},\end{aligned} \tag{68}$$

$$\begin{aligned}p = \mu\Bigg\{&\frac{1}{6}\left(\frac{R}{r\lambda\beta}\right)^2 - \frac{1}{3}\left(\frac{r\beta}{R}\right)^2 - \frac{1}{3}\lambda^2 + \frac{A^2}{2(\lambda\beta a)^2} \\ &+ \frac{1}{2\lambda\beta}\ln\frac{r^2}{a^2} - \frac{\beta}{2\lambda}\ln\left\{\frac{\lambda\beta}{B^2 - A^2}[b^2 - r^2 + \frac{B^2}{A^2}(r^2 - a^2)]\right\}\Bigg\}.\end{aligned} \tag{69}$$

From Eq. (68),

$$T_{\theta\theta}(r=a)=\mu\Big[\frac{(\beta a)^2}{A^2}-\frac{A^2}{(\lambda\beta a)^2}\Big]$$

and

$$T_{\theta\theta}(r=b)=\mu\Big\{\frac{(\beta b)^2}{B^2}-\frac{B^2}{2(\lambda\beta b)^2}-\frac{A^2}{2(\lambda\beta a)^2}+\frac{\beta}{\lambda}\ln\frac{B}{A}-\frac{1}{\lambda\beta}\ln\frac{b}{a}\Big\},$$

with b given by Eq. (44) and β to be obtained as a function of a by solving Eq. (66).

Also, note that the conditions (65) allow the integration of the balance law (63) while ensuring that the axial force along the circumferential direction vanishes, as

$$\int_a^b T_{\theta\theta}\mathrm{d}r=bT_{rr}(b,t)-aT_{rr}(a,t)=0\,.$$

From Eqs. (62) and (69), the final expression for the normal out-of-plane stress is

$$T_{zz}=\frac{\mu}{2\lambda\beta}\Big\{-1-\frac{1}{Hr^2}(Ab^2-Ba^2)+\frac{A}{\lambda\beta}\Big(\frac{B}{r^2}-\frac{A}{a^2}\Big)+2\lambda^3\beta-\ln\frac{r^2}{a^2}+\beta^2\ln\Big[\lambda\beta\Big(\frac{r^2}{A^2}+\frac{A^2b^2-B^2a^2}{A^2(B^2-A^2)}\Big)\Big]\Big\}\,.$$

Finally, λ is determined either to be equal to 1 by assuming plane-strain conditions, or by imposing a prescribed value for the axial force normal to the sector face of outward normal $\pm\mathbf{e}_z$. Selecting zero for such a value yields

$$\int_a^b T_{zz}r\mathrm{d}r=0\,,$$

which is denoted as "axially-free" condition in the following and leads to

$$2\lambda\beta\Big(\beta^2\ln\frac{B}{A}-\ln\frac{b}{a}\Big)=\Big(1-\frac{A^2}{B^2}\Big)\Big[\frac{A^2}{a^2}+\lambda\beta^2(\beta-2\lambda^3)\Big]\,. \tag{70}$$

So, substitution of Eq. (44) in Eqs. (66) and (70) leads to a nonlinear algebraic system of two equations to be solved for β and λ as functions of a^2, where a is assumed to be the loading parameter.[3]

Under plane strain, $\lambda=1$ and the solution is obtained by disregarding Eq. (70) and solving Eq. (66) only.

The bending moment per unit initial depth applied to an edge with unit outer normal $\mathbf{n}=\mathbf{e}_\theta$ is given by

$$\mathbf{M}=M\mathbf{e}_z\,,\quad M=\lambda\int_a^b T_{\theta\theta}r\mathrm{d}r\,, \tag{71}$$

such as for $M>0$ the inner and outer regions of the circular sector are, respectively, under circumferential compression and circumferential tension.

By using Eqs. (68) and (44), the bending moment per unit initial depth in Eq. (71) is obtained as

$$M=\mu\Big\{\frac{B^2-A^2}{4\lambda}+\frac{1}{2\lambda}[B^2-2A^2+2a^2\lambda\beta]\ln\frac{B}{A}-\frac{B^2-A^2}{4\lambda^2\beta^3}\Big(\frac{A}{a}\Big)^2-\frac{B^2}{4\lambda\beta^2}\ln\Big(1+\frac{B^2-A^2}{\lambda\beta a^2}\Big)\Big\}\,. \tag{72}$$

[3] An alternative and convenient solution scheme consists of assigning β and solving Eq. (67) for h/a, then, using Eq. (44) to obtain

$$\hat\lambda_a\equiv\lambda a^2=\frac{B^2-A^2}{\beta(h^2/a^2+2h/a)}\,,$$

then, using Eq. (70) to obtain as the real root of

$$\lambda=\Big\{\frac{A^2}{2\hat\lambda_a\beta^2}+\frac{\beta}{2}+\frac{B^2}{\beta(B^2-A^2)}\Big[\ln\Big(1+\frac{h}{a}\Big)-\beta^2\ln\frac{B}{A}\Big]\Big\}^{1/3}\,,$$

and, finally, computing $a=\sqrt{\hat\lambda_a/\lambda}$. Although such a procedure suggests using β as loading parameter instead of a, this does not hold in the elastoplastic case, where, as it will be explained in Appendix A, it is more convenient to apply a. For definiteness, $a(t)$ is used as loading parameter for all examples.

4.3.1. Illustration of the elastic behavior under large deformations

Figs. 2, 3, 4, and 5 illustrate the large-deformation elastic bending response for both the axially-free and plane-strain cases by plotting, as a function of $\log_{10}(a/A)$, the structural stretches β,λ, and the current thickness h, the latter being normalized by either H or a. By providing results both for $H/A=0.001, B/A=1.001$ (Figs. 2 and 3) and for $H/A=1., B/A=2.$ (Figs. 4 and 5), these two analyses demonstrate the huge effect on the response of the initial relative thickness H/A, which influences the response for a given H.

In both analyses β increases up to 1000 and this corresponds to a dramatic decrease of a. The average through-the-thickness stretch h/H shows that the thickness diminishes in order to satisfy the incompressibility constraint (44). The ratio h/a instead shows that by decreasing a the curved plate may become much "thicker" in the sense of the terminology of structural mechanics. The results also show that for the thin sector, $H/A=0.001, B/A=1.001$, λ remains very close to 1 (Fig. 2(b)). Consequently, the results obtained for the thin sector are a good approximation of the solution for the plane-strain case. In contrast, for the case of the thick sector, $H/A=1., B/A=2.$, λ increases up to ≈6.5 (Fig. 4(b)), which indicates a significant discrepancy with respect to the plane-strain problem, as displayed with the red dashed curves in Figs. 4(a) and 5. The comparison between the axially-free and plane-strain results shows that the out-of-plane condition has a mild influence on the solution and, obviously, that the plane-strain response is stiffer, as, for a given $\beta>1$, both a and h decrease less with respect to A and H than in the axially-free case.

Finally, Fig. 6 displays, for the two considered circular sectors, h/a as a function of β, that is the solution of Eq. (67), which holds exactly for any value of λ (so, including both axially-free and plane-strain conditions). From this figure it is observed that when h/a becomes large, as it is surely the case for the thick sector, the relation between h/a and β is almost linear, as, in fact, in Eq. (67), the term $(h/a)^2$ in the first numerator dominates over other contributions involving h/a, such as the solution can be approximated by

$$\frac{h}{a}\approx\Big(\frac{\sqrt{B^2-A^2}}{A}\ln\frac{B^2}{2A^2}\Big)\beta\,.$$

In the plane-strain elastoplastic case solved in Section 4.4.4, a structurally neither too-thin nor too-thick sector will be considered, specifically characterized by

$$B/A=1.1\,,\quad H/A=0.1,$$

and the inner radius will be decreased up to A/100. For comparison, the elastic solution for this benchmark provides

$$\beta\approx37.5\,,\quad h/a\approx6.56\,. \tag{73}$$

4.4. The crystallography: symmetric double slip

As depicted in Fig. 1, the plastic deformation rate is assumed to develop by following symmetric double slip, with the two slip systems specified such that they have identical transverse directions ${}_I\mathbf{t}$, as

$$\begin{aligned}&{}_1\mathbf{s}=\sin(\alpha)\mathbf{e}_r+\cos(\alpha)\mathbf{e}_\theta\,,\quad {}_1\mathbf{n}=-\cos(\alpha)\mathbf{e}_r+\sin(\alpha)\mathbf{e}_\theta\,,\quad {}_1\mathbf{t}=\mathbf{e}_z\,,\\ &{}_2\mathbf{s}=\sin(\alpha)\mathbf{e}_r-\cos(\alpha)\mathbf{e}_\theta\,,\quad {}_2\mathbf{n}=\cos(\alpha)\mathbf{e}_r+\sin(\alpha)\mathbf{e}_\theta\,,\quad {}_2\mathbf{t}=\mathbf{e}_z\,.\end{aligned} \tag{74}$$

With this crystallography, by selecting identical material parameters for the two slip systems, thus, with reference to Eqs. (32), (34), and (35), denoting

$$\begin{aligned}&{}_1b={}_2b=b_\Gamma\,,\quad {}_1m_H={}_2m_H=m_H\,,\quad {}_1Y_{H0}={}_2Y_{H0}=Y_{H0}\,,\\ &{}_1Y_{Hs}={}_2Y_{Hs}=Y_{Hs}\,,\quad {}_1m_\ell={}_2m_\ell=m_\ell\,,\quad {}_1m_r={}_2m_r=m_r\,,\\ &{}_1Y_{Rs}={}_2Y_{Rs}=Y_{Rs}\,,\quad {}_1n_R={}_2n_R=n_R\,,\end{aligned} \tag{75}$$

elastoplastic bending is characterized by

$${}_1\Gamma=-{}_2\Gamma=\Gamma\,, \tag{76}$$

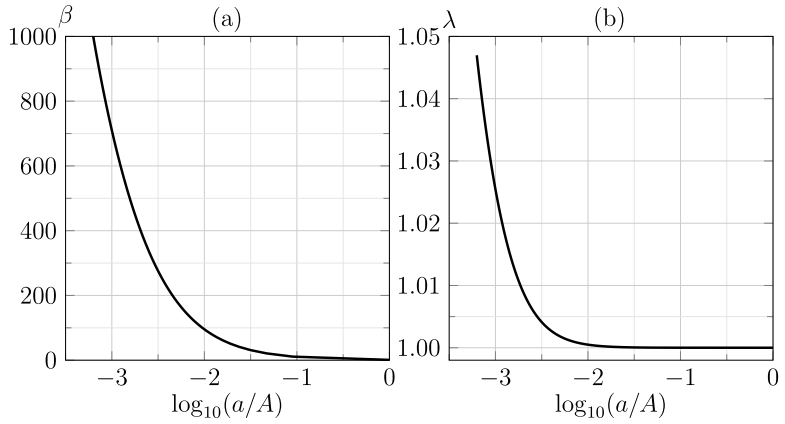

Fig. 2. Large-deformation elastic bending of a "thin" sector ($B/A = 1.001$, $H/A = 0.001$): circumferential stretch β (a) and out-of-plane stretch λ (b) as functions of the normalized current radius a/A in a logarithmic scale.

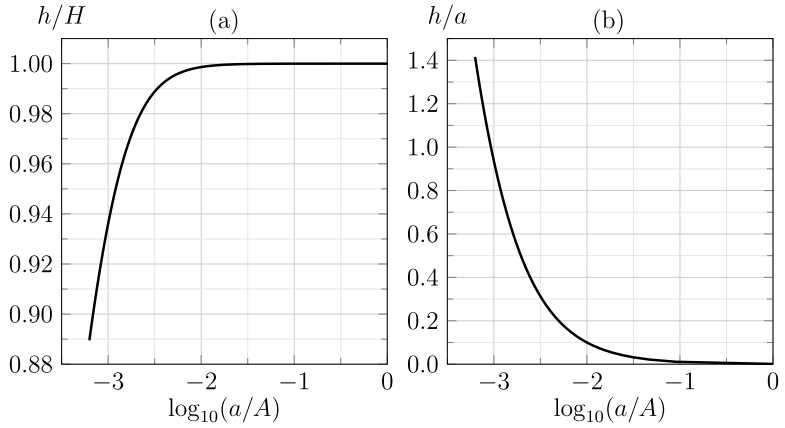

Fig. 3. Evolution of the current thickness $h = b - a$ in large-deformation elastic bending of a "thick" sector ($B/A = 1.001$, $H/A = 0.001$): h/H (a) and h/a (b) as functions of the normalized current radius a/A in a logarithmic scale.

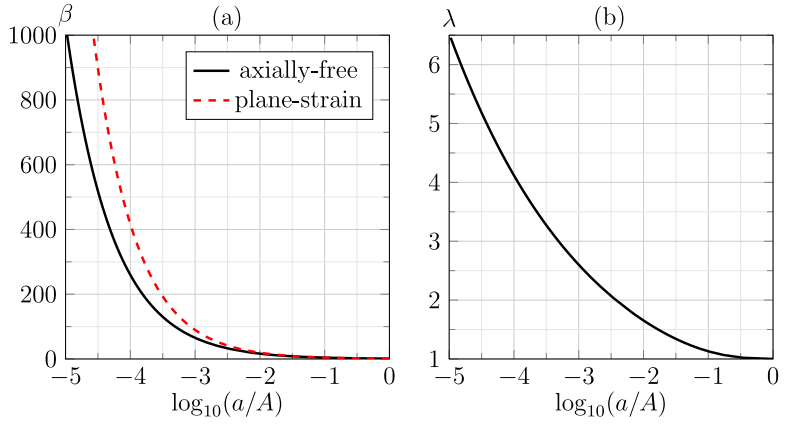

Fig. 4. Large-deformation elastic bending of a "thick" sector ($B/A = 2.$, $H/A = 2.$): circumferential stretch β (a) and out-of-plane stretch λ (b) as functions of the normalized current radius a/A in a logarithmic scale.

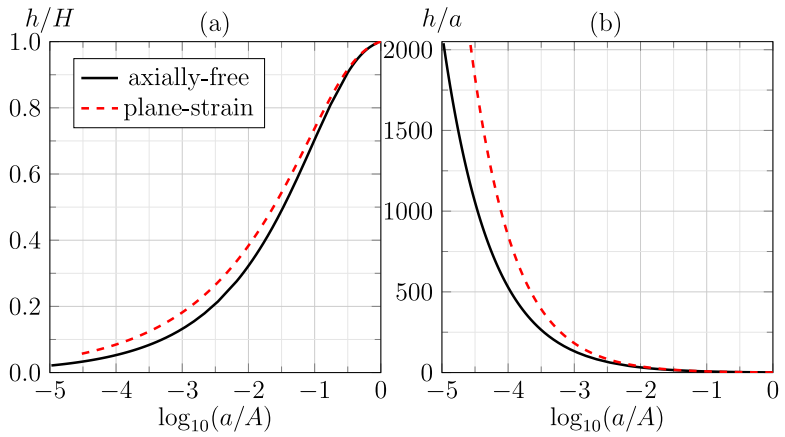

Fig. 5. Evolution of the current thickness $h = b - a$ in large-deformation elastic bending of a "thick" sector ($B/A = 2.$, $H/A = 2.$): h/H (a) and h/a (b) as functions of the normalized current radius a/A in a logarithmic scale.

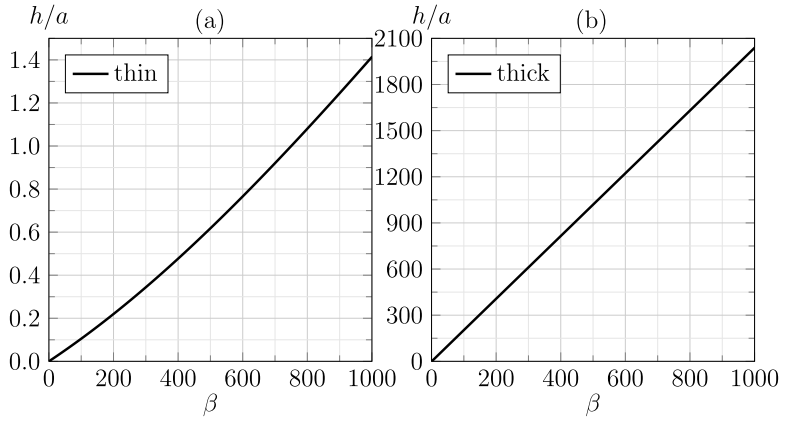

Fig. 6. Evolution of the current thickness $h = b - a$ relative to the current inner radius a in large-deformation elastic bending for (a) "thin" ($B/A = 1.001\,, H/A = 0.001$) and (b) "thick" ($B/A = 2.\,, H/A = 1.$) circular sectors as functions of the circumferential stretch β. Note that, in the light of Eq. (67), these results also exactly hold under plane-strain conditions.

along with

$$ {}_1Y_\ell = {}_2Y_\ell = Y_\ell\,, \quad {}_1Y_H = {}_2Y_H = Y_H\,, \quad {}_1Y_R = {}_2Y_R = Y_R\,, \tag{77} $$

and the plastic rate in Eq. (7) specializes to

$$ \mathbf{L}_p'' = \Gamma\sin(2\alpha)(-\mathbf{e}_r\otimes\mathbf{e}_r + \mathbf{e}_\theta\otimes\mathbf{e}_\theta)\,, \tag{78} $$

which is, of course, consistent with plane-strain isochoric bending deformation and shows that the definition (76) implies that a positive Γ corresponds to a positive direct plastic strain rate along the circumferential direction. Importantly, note that, under the assumed kinematics (39), symmetric double slip leads to vanishing plastic spin rate. On the one hand, this is unfortunate, as the plastic spin may largely contribute to the incompatibility (see, e.g., Bardella, 2009; Bardella and Panteghini, 2015; Poh and Peerlings, 2016; Rubin and Bardella, 2024, and references therein). On the other hand, because of this, Eqs. (57)–(59) still hold in the elastoplastic case. A crystallography allowing for non-vanishing plastic spin rate would break the symmetry that allows the boundary value problem to be spatially one-dimensional, thus enormously increasing its difficulty. As an example, in Appendix B the basic equations for the case of single slip are provided.

Furthermore, by using Eqs. (9) and (57) and by taking $\alpha = \alpha_z$ in a RLS, from Eq. (74) it follows that

$$
\begin{aligned}
&{}_1s^1 = \sin(\alpha_z)\,, \quad {}_1s^2 = \cos(\alpha_z)\,, \quad {}_1s^3 = 0\,,\\
&{}_1n_1 = -\cos(\alpha_z)\,, \quad {}_1n_2 = \sin(\alpha_z)\,, \quad {}_1n_3 = 0\,,\\
&{}_2s^1 = \sin(\alpha_z)\,, \quad {}_2s^2 = -\cos(\alpha_z)\,, \quad {}_2s^3 = 0\,,\\
&{}_2n_1 = \cos(\alpha_z)\,, \quad {}_2n_2 = \sin(\alpha_z)\,, \quad {}_2n_3 = 0\,,\\
&{}_1\mathbf{s} = \frac{1}{\mathcal{M}(\alpha_z)}[\sin(\alpha_z)m'_{1r}\mathbf{e}_r + \cos(\alpha_z)m'_{2\theta}\mathbf{e}_\theta]\,,\\
&{}_1\mathbf{n} = \frac{1}{\mathcal{M}(\alpha_z)}[-\cos(\alpha_z)m'_{2\theta}\mathbf{e}_r + \sin(\alpha_z)m'_{1r}\mathbf{e}_\theta]\,, \quad {}_1\mathbf{t}_1 = \mathbf{e}_z\,,\\
&{}_2\mathbf{s} = \frac{1}{\mathcal{M}(\alpha_z)}[\sin(\alpha_z)m'_{1r}\mathbf{e}_r - \cos(\alpha_z)m'_{2\theta}\mathbf{e}_\theta]\,,\\
&{}_2\mathbf{n} = \frac{1}{\mathcal{M}(\alpha_z)}[\cos(\alpha_z)m'_{2\theta}\mathbf{e}_r + \sin(\alpha_z)m'_{1r}\mathbf{e}_\theta]\,, \quad {}_1\mathbf{t}_2 = \mathbf{e}_z\,,\\
&\sin(\alpha) = {}_1\mathbf{s}\cdot\mathbf{e}_r = {}_2\mathbf{s}\cdot\mathbf{e}_r = \frac{\sin(\alpha_z)m'_{1r}}{\mathcal{M}(\alpha_z)}\,,\\
&\text{with} \quad \mathcal{M}(\alpha_z) = \sqrt{\left[\sin(\alpha_z)m'_{1r}\right]^2 + \left[\cos(\alpha_z)m'_{2\theta}\right]^2}\,.
\end{aligned}
\tag{79}
$$

Because of Eq. (74), Eq. (17) specializes to

$$
\begin{aligned}
&{}_1\mathbf{s}\otimes\operatorname{curl}({}_1\mathbf{n}) + (\partial_1\mathbf{s}/\partial\mathbf{x})({}_1\mathbf{s}\otimes\mathbf{e}_z - \mathbf{e}_z\otimes{}_1\mathbf{s})\\
&= \left[\left(\frac{\sin^2(\alpha)}{r} + \sin(2\alpha)\frac{\partial\alpha}{\partial r}\right)\mathbf{e}_r + \left(\frac{\sin(2\alpha)}{2r} + \cos(2\alpha)\frac{\partial\alpha}{\partial r}\right)\mathbf{e}_\theta\right]\otimes\mathbf{e}_z\,.
\end{aligned}
$$

$$
{}_2\mathbf{s}\otimes\operatorname{curl}({}_2\mathbf{n})+(\partial_2\mathbf{s}/\partial\mathbf{x})({}_2\mathbf{s}\otimes\mathbf{e}_z-\mathbf{e}_z\otimes{}_2\mathbf{s})
$$
$$
=\left[\left(\frac{\sin^2(\alpha)}{r}+\sin(2\alpha)\frac{\partial\alpha}{\partial r}\right)\mathbf{e}_r-\left(\frac{\sin(2\alpha)}{2r}+\cos(2\alpha)\frac{\partial\alpha}{\partial r}\right)\mathbf{e}_\theta\right]\otimes\mathbf{e}_z\,.
$$

Therefore, using Eq. (76) yields

$$
\sum_{I=1}^{2}{}_I\Gamma\operatorname{curl}({}_I\mathbf{s}\otimes{}_I\mathbf{n})=2\Gamma\left(\frac{\sin(2\alpha)}{2r}+\cos(2\alpha)\frac{\partial\alpha}{\partial r}\right)\mathbf{e}_\theta\otimes\mathbf{e}_z\,. \tag{80}
$$

The contribution to $\operatorname{curl}(\mathbf{L}_p)$ in Eq. (16) due to pure densities of GNDs, to be compared with the contribution in Eq. (80), obviously depends on densities of pure edge dislocations only, as ${}_I\dot\rho_\odot=-{}_I\Gamma_{,k}({}_I\mathbf{t}\cdot\mathbf{g}^k)=-(\partial_I\Gamma/\partial r)\mathbf{e}_z\cdot\mathbf{e}_r=0$, and reads

$$
\sum_{I=1}^{2}{}_I\dot\rho_{\perp I}\mathbf{s}\otimes{}_I\mathbf{t}=\frac{\partial\Gamma}{\partial r}\sin(2\alpha)\mathbf{e}_\theta\otimes\mathbf{e}_z\,. \tag{81}
$$

Thus, summing up Eqs. (80) and (81) for the symmetric double slip studied here yields

$$
\operatorname{curl}(\mathbf{L}_p)=\left[2\Gamma\left(\frac{\sin(2\alpha)}{2r}+\cos(2\alpha)\frac{\partial\alpha}{\partial r}\right)+\frac{\partial\Gamma}{\partial r}\sin(2\alpha)\right]\mathbf{e}_\theta\otimes\mathbf{e}_z\,. \tag{82}
$$

By combining Eqs. (3) and (82) the single non-vanishing Eulerian rate of elastic incompatibility reads

$$
\begin{aligned}
&R_{23}=R_{23}^{\mathrm{GND}}+R_{23}^{\mathrm{ed}}\,,\\
&R_{23}^{\mathrm{GND}}=\frac{\partial\Gamma}{\partial r}\sin(2\alpha)m'_{2\theta}m'_{3z}\,,\\
&R_{23}^{\mathrm{ed}}=2\Gamma\left(\frac{\sin(2\alpha)}{2r}+\cos(2\alpha)\frac{\partial\alpha}{\partial r}\right)m'_{2\theta}m'_{3z}\,.
\end{aligned} \tag{83}
$$

4.4.1. Lattice rotation in the purely elastic regime

By assuming that slip systems are never activated, that is $|{}_I\gamma_e|$ never reaches ${}_IY$, see Eq. (32), it is possible to study the evolution of the slip systems orientation α due to elastic deformation, which, for certain materials, might be useful in the light of its contribution to the incompatibility in Eq. (83).

Combining the last two relations in Eq. (79) with the results in Eqs. (43) and (61) yields

$$
\alpha=\sin^{-1}\frac{\sin(\alpha_z)}{\sqrt{\sin^2(\alpha_z)+\cos^2(\alpha_z)\beta^2\left(1+\dfrac{\lambda\beta a^2-A^2}{R^2}\right)}}\,. \tag{84}
$$

For the initial value $\alpha_z=30°$, Fig. 7 displays the evolution of α by plotting the function $\alpha(R)$ for different values of β and for the thin, $B/A=1.001\,,H/A=0.001$, and thick, $B/A=2\,,H/A=1$, sectors considered in Section 4.3. It is observed that for the thin sector very large values of β are required for α to significantly depart from α_z. Instead, for the thick sector, $\beta=4$ is enough to obtain $\alpha\approx70°$ at the inner radius; moreover, by increasing β, see the case $\beta=100$ in Fig. 7(b), $\alpha(R=A)$ and $\alpha(R=B)$ tend to 90° and 0°, respectively, with the region of large α localized towards the inner radius. It is important to notice that such a localization is, actually, not as pronounced as one might deduce from Fig. 7(b), as is observable in Fig. 8(a), showing the behavior of α as a function of the Eulerian coordinate r. Additionally, for the largest deformation, $\beta=100$, of the thick sector, Fig. 8(b) shows the very large influence on the circumferential stress of the out-of-plane condition. Specifically, at $r=a$, which is the most stressed point, $T_{\theta\theta}(a)/\mu$ is equal to ≈-41.2 in the axially-free case, against ≈-138 in the plane-strain case. Also, $T_{\theta\theta}$ experiences a large gradient in a thin boundary layer region with inner edge $r=a$. These extremely large values of $T_{\theta\theta}(a)/\mu$ are of course due to the severe elastic deformations experienced by the sectors in these examples.

Finally, with reference to Fig. 8(a), note that from inspection of Eqs. (84) and (43), specifically by observing that

$$
\lambda\beta a^2=\frac{R^2-A^2}{(r/a)^2-1}\,,
$$

it is deduced that the function $\alpha(r/a)$ is independent of the out-of-plane condition, causing it to be the same under plane-strain and axially-free conditions.

4.4.2. Elastoplastic evolution equations for the distortional microstructural vectors

In the light of the results of Section 4.3 and in order to simplify the equations to solve in the elastoplastic case, it is convenient to resort to plane-strain conditions, such that

$$
\lambda=1
$$

is henceforth always assumed.

Then, using Eqs. (57)–(59), the evolution equations in (5) require

$$
\begin{aligned}
&\frac{\dot m'_{1r}}{m'_{1r}}\mathbf{e}_r=-\left(\frac{\dot r}{r}+\frac{\dot\beta}{\beta}\right)\mathbf{e}_r-\mathbf{L}''_p\mathbf{e}_r\,,\\
&\frac{\dot m'_{2\theta}}{m'_{2\theta}}\mathbf{e}_\theta=\left(\frac{\dot r}{r}+\frac{\dot\beta}{\beta}\right)\mathbf{e}_\theta-\mathbf{L}''_p\mathbf{e}_\theta\,,\\
&\frac{\dot m'_{3z}}{m'_{3z}}\mathbf{e}_z=-\mathbf{L}''_p\mathbf{e}_z\,.
\end{aligned} \tag{85}
$$

The form of the plastic rate in Eq. (78) for the selected symmetric double slip allows Eq. (85) to be simplified as

$$
\begin{aligned}
&\frac{\dot m'_{1r}}{m'_{1r}}=-\left(\frac{\dot r}{r}+\frac{\dot\beta}{\beta}\right)+\Gamma\sin(2\alpha)\,,\\
&\frac{\dot m'_{2\theta}}{m'_{2\theta}}=\left(\frac{\dot r}{r}+\frac{\dot\beta}{\beta}\right)-\Gamma\sin(2\alpha)\,,\\
&\frac{\dot m'_{3z}}{m'_{3z}}=0\,,
\end{aligned} \tag{86}
$$

that is

$$
\begin{aligned}
&\frac{\dot m'_{1r}}{m'_{1r}}=-\left(\frac{\dot r}{r}+\frac{\dot\beta}{\beta}\right)+\Gamma\sin(2\alpha)\,,\quad m'_{2\theta}=\frac{1}{m'_{1r}}\,,\quad m'_{3z}=1\,,\\
&\text{with}\quad \sin(\alpha)=\frac{\sin(\alpha_z)m'^2_{1r}}{\sqrt{\sin^2(\alpha_z)m'^4_{1r}+\cos^2(\alpha_z)}}\,,
\end{aligned} \tag{87}
$$

the latter relation being obtained by using the last two expressions in Eq. (79). Therefore, Eq. (83) becomes

$$
\begin{aligned}
&R_{23}=R_{23}^{\mathrm{GND}}+R_{23}^{\mathrm{ed}}\,,\\
&R_{23}^{\mathrm{GND}}=\frac{\partial\Gamma}{\partial r}\sin(2\alpha)\frac{1}{m'_{1r}}\,,\\
&R_{23}^{\mathrm{ed}}=2\Gamma\left(\frac{\sin(2\alpha)}{2r}+\cos(2\alpha)\frac{\partial\alpha}{\partial r}\right)\frac{1}{m'_{1r}}\,.
\end{aligned} \tag{88}
$$

The unknown current radial coordinate field can be eliminated from Eq. (87) by using Eq. (43) as

$$
\frac{\dot r}{r}=\frac{a}{a^2+\frac{R^2-A^2}{\beta}}\dot a-\frac{R^2-A^2}{2\beta^2\left(a^2+\frac{R^2-A^2}{\beta}\right)}\dot\beta\,. \tag{89}
$$

Moreover, by specifying $a(t)$ as the loading parameter, β becomes a function of a to be determined, i.e.

$$
\dot\beta=\frac{\mathrm{d}\beta}{\mathrm{d}a}\dot a\,,
$$

and Eq. (87) becomes

$$
\frac{1}{m'_{1r}}\frac{\partial m'_{1r}}{\partial a}=-\underbrace{\left[\frac{a}{a^2+\frac{R^2-A^2}{\beta}}+\left(\frac{a^2}{a^2+\frac{R^2-A^2}{\beta}}+1\right)\frac{1}{2\beta}\frac{\mathrm{d}\beta}{\mathrm{d}a}\right]}_{\mathcal{F}(R,a)}+\frac{\Gamma\sin(2\alpha)}{\dot a}\,. \tag{90}
$$

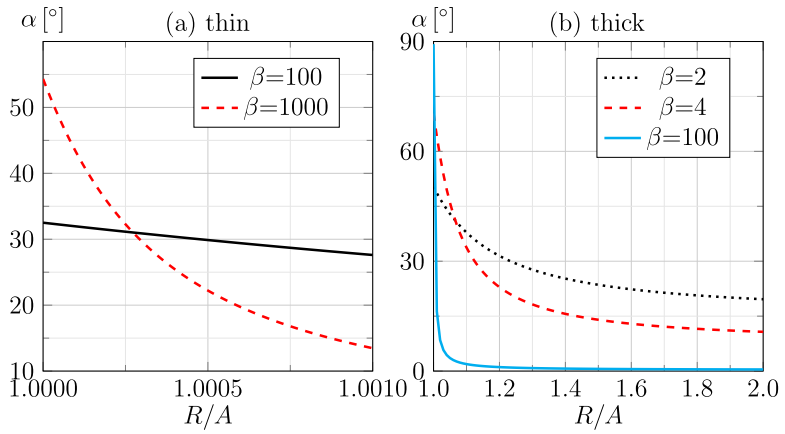

Fig. 7. Evolution of the crystallographic angle α, with $\alpha_z = 30°$, relative to the circumferential stretch β in large-deformation elastic bending for (a) "thin" ($B/A = 1.001\,, H/A = 0.001$) and (b) "thick" ($B/A = 2.\,, H/A = 1.$) circular sectors as functions of the non-dimensional nominal radial coordinate R/A.

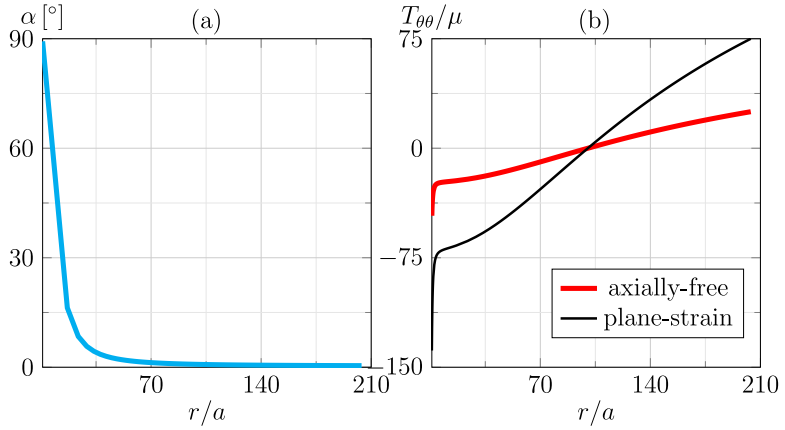

Fig. 8. The crystallographic angle α, with $\alpha_z = 30°$, (a) and the non-dimensional circumferential stress $T_{\theta\theta}/\mu$ (b) for circumferential stretch $\beta = 100$ in large-deformation elastic bending for the "thick" ($B/A = 2.\,, H/A = 1.$) circular sector as functions of the normalized current radial coordinate r/a. Note that the result for α in (a) holds exactly the same for both the axially-free and the plane-strain cases.

With the help of Eqs. (28), (31), (57), (74), and (87) it can be shown that

$$\begin{aligned}
&\mathbf{B}''_e = B''_{err}\mathbf{e}_r\otimes\mathbf{e}_r + B''_{e\theta\theta}\mathbf{e}_\theta\otimes\mathbf{e}_\theta + B''_{ezz}\mathbf{e}_z\otimes\mathbf{e}_z\,,\\
&B''_{err} = \frac{2m'^2_{1r}}{3} - \frac{1}{3m'^2_{1r}} - \frac{1}{3}\,,\quad B''_{e\theta\theta} = -\frac{m'^2_{1r}}{3} + \frac{2}{3m'^2_{1r}} - \frac{1}{3}\,,\\
&B''_{ezz} = -\frac{m'^2_{1r}}{3} - \frac{1}{3m'^2_{1r}} + \frac{2}{3}\,,\quad {}_1\gamma_e = -{}_2\gamma_e = \gamma_e = \frac{1-m'^4_{1r}}{2m'^2_{1r}}\sin(2\alpha)\,.
\end{aligned}\tag{91}$$

Because of Eqs. (56), (74), and (75), from Eqs. (77) and (83) it follows that the smooth transition for the plastic slip rate in Eq. (32) reduces to

$$\Gamma = b_\Gamma\left|\left(\frac{\dot r}{r} + \frac{\dot\beta}{\beta}\right)\sin(2\alpha)\right|\langle|\gamma_e| - Y\rangle\frac{\gamma_e}{|\gamma_e|}\,,$$

which can be rewritten as

$$\Gamma = b_\Gamma\left|\mathcal{F}(R,a)\dot a\sin(2\alpha)\right|\langle|\gamma_e| - Y\rangle\frac{\gamma_e}{|\gamma_e|}\,.\tag{92}$$

Additionally, the hardening equations in (34) reduce to

$$\begin{aligned}
&Y = Y_H + Y_\ell\,,\quad \dot Y_H = |\Gamma|m_H(Y_{Hs} - Y_H)\,,\\
&\dot\xi = \dot\xi^{\rm GND} + \dot\xi^{\rm ed}\,,\quad \dot\xi^{\rm GND} = \ell R^{\rm GND}_{23}\,,\quad \dot\xi^{\rm ed} = \ell R^{\rm ed}_{23}\,,\\
&\dot Y_\ell = |\dot\xi|\left[m_\ell\langle Y_R - Y_\ell\rangle - m_r\langle Y_\ell - Y_R\rangle\right]\,,\quad Y_R = Y_{Rs}\,(1-10^{-|\xi|})^{n_R}\,.
\end{aligned}\tag{93}$$

4.4.3. Equilibrium equations and boundary conditions

Using the results (91), Eq. (28), and the second relation in the constitutive equation in (30) it follows that, because of incompressibility,

$$\begin{aligned}
&\mathbf{T} = T_{rr}\mathbf{e}_r\otimes\mathbf{e}_r + T_{\theta\theta}\mathbf{e}_\theta\otimes\mathbf{e}_\theta + T_{zz}\mathbf{e}_z\otimes\mathbf{e}_z\,,\\
&T_{rr} = -p + \mu B''_{err}\,,\quad T_{\theta\theta} = -p + \mu B''_{e\theta\theta}\,,\quad T_{zz} = -p + \mu B''_{ezz}\,,\\
&T_{rr} - T_{\theta\theta} = \mu\left(m'^2_{1r} - \frac{1}{m'^2_{1r}}\right),
\end{aligned}\tag{94}$$

which are functions of r and the loading parameter $a(t)$. Moreover, due to the incompressibility constraint, p is a function of (r,a) that is determined by equilibrium and boundary conditions. Consequently, in the absence of body force and neglecting accelerations, the sole non-trivial equilibrium equation, Eq. (63), can be written in the form

$$\frac{\partial T_{rr}}{\partial r} = \frac{\mu}{r}\left(\frac{1}{m'^2_{1r}} - m'^2_{1r}\right),\tag{95}$$

which, by using Eq. (43), can be rewritten as

$$\frac{\partial T_{rr}}{\partial R} = \frac{\mu\left(\frac{1}{m'^2_{1r}} - m'^2_{1r}\right)R}{\beta a^2 + R^2 - A^2}\,,\tag{96}$$

to be solved by imposing the Lagrangian form of the boundary conditions in Eq. (65), i.e.

$$T_{rr}(A,t) = 0\,,\quad T_{rr}(B,t) = 0\,.\tag{97}$$

The elastoplastic problem has been solved numerically as reported in Algorithm 1 and explained in more detail in Appendix A.

Algorithm 1 Algorithm for numerical integration

Assign $a(t)$ with $a(t=0)=a_0\equiv A$, set a trial value for $\beta(t)=\beta(t_n)$

while do

for each material point $R_j\in[A,B]$, with $j=1..n_R+1$ **do**

1. Compute

$$\mathcal{F}_j=\frac{a}{a^2+\frac{R_j^2-A^2}{\beta}}+\left(\frac{a^2}{a^2+\frac{R_j^2-A^2}{\beta}}+1\right)\frac{1}{2\beta}\frac{\Delta\beta}{\Delta a}\,,$$

2. Compute $(m'_{1r})_j$, α_j, $(\gamma_e)_j$, Γ_j as a function of $\mathcal{F}_j$ and of the hardening variables $Y_j(t_n)$ at the previous time step by numerically solving the nonlinear scalar equation (A.1)
3. Compute

$$\left(\frac{\partial T_{rr}}{\partial R}\right)_j=\frac{\mu\left(\frac{1}{\left(m'^2_{1r}\right)_j}-\left(m'_{1r}\right)_j^2\right)R_j}{\beta a^2+R_j^2-A^2}$$

end for

for $j=1,n_R-1$ step 2 **do**

Compute $(T_{rr})_j$, with $(T_{rr})_1=0$ using the Simpson's rule

$$(T_{rr})_{j+2}=(T_{rr})_j+\frac{R_{j+2}-R_j}{6}\left[\left(\frac{\partial T_{rr}}{\partial R}\right)_j+4\left(\frac{\partial T_{rr}}{\partial R}\right)_{j+1}+\left(\frac{\partial T_{rr}}{\partial R}\right)_{j+2}\right]$$

end for

if $|T_{rr}(B)|=\left|(T_{rr})_{n_R+1}\right|<\epsilon$ **then** exit while loop

else

$$\beta_{new}=\beta-(T_{rr})_{n_R+1}\Big/\left(\frac{\partial T_{rr}}{\partial\beta}\right)_{n_R+1}$$

end if

end while

for each $R_j\in[A,B]$ **do**

Compute the spatial derivatives of α_j and Γ_j and $\left(m'_{1r}\right)_j$ as functions of $\partial\mathcal{F}_j/\partial R$ by numerically solving the implicit equation obtained by differentiating Eqs. (A.1) and (A.2) with respect to the space

Update $Y_{\ell,j}(t)$ and $Y_j(t)$ by applying Backward Euler rule to Eqs. (93)

end for

4.4.4. Discussion of the results

The sample shape and crystallography are defined by

$$H/A=0.1\,,\quad B/A=1.1\,,\quad \alpha_z=\pi/6\,.$$

The material parameters governing the size-independent response of the model are selected as

$$\mu=44\text{ GPa}\,,\ b_\Gamma=3000\,,\ Y_{H0}=2\times10^{-3}\,,\ Y_{Hs}=3\times10^{-3}\,,\ m_H=20\,,\tag{98}$$

except for perfect plasticity, in which $m_H=0$. The adopted value for b_Γ is adequate for metals, where the overstress is relatively small, and $\mu=44$ GPa is specific of copper. The material parameters governing the size-dependent response that are kept fixed in the following analyses are

$$m_H=20\,,\quad m_\ell=15\,,\quad Y_{Rs}=3\times10^{-3}\,,\quad n_R=0.3\,,$$

while results will be discussed by varying both m_r, which controls the rate of recovery of size-dependent hardening, and, more importantly, the size of the sample by considering different values of the parameter A/ℓ.

The loading consists of decreasing the inner radius to $a_{\min}\equiv a(t_0)=A/100$ and, then, reverse loading by expanding a to its initial value A.

Table 1
Elastoplastic response of a circular sector with $B/A=1.1$, $H/A=0.1$, $\alpha_z=\pi/6$: Values for circumferential stretch β and normalized current thickness h/a at the end of the loading ramp (i.e. for final inner radius $a=a_{\min}=A/100$) for different samples sizes with hardening parameter $m_r=1$.

Sample	β	h/a
$b_\Gamma=0$	37.5	6.56
$A/\ell\to\infty$, $m_H=0$	18.9	9.58
$A/\ell\to\infty$	19.4	9.45
$A/\ell=1000$	20.1	9.26
$A/\ell=100$	21.4	8.96
$A/\ell=10$	20.2	9.24
$A/\ell=1$	19.9	9.31

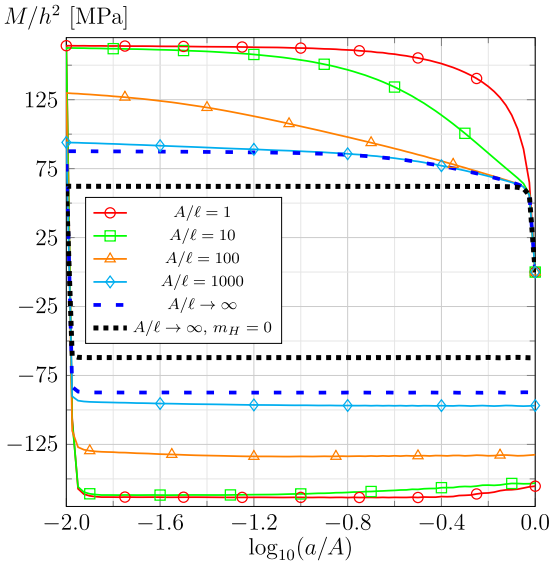

Fig. 9. Normalized bending moment vs. non-dimensional applied internal radius a/A in the elastoplastic response of a circular sector with $B/A=1.1$, $H/A=0.1$, $\alpha_z=\pi/6$: Comparison of the predictions for different sample sizes for loading and reverse loading with hardening parameter $m_r=1$. The case of conventional perfect plasticity, $A/\ell\to\infty$, $m_H=0$, is displayed for comparison.

The fictitious time t_0 indicates how long it takes to reach $a_{\min}$ in the loading ramp, but the response is rate-independent.

Table 1 shows the comparison in terms of β and h/a at the end of the loading ramp with the results reported in Eq. (73) for the elastic solution ($b_\Gamma=0$). A stark difference is observed between the elastic and the elastoplastic solutions, the latter ranging from conventional perfect plasticity ($A/\ell\to\infty\,,m_H=0$) to size-dependent plasticity in a very small sample ($A/\ell=1$). Note also that β and h/a do not vary much with the sample size in the considered elastoplastic cases, thus suggesting that they depend on the initial yield point through the parameter Y_{H0}. Additionally, both β and h/a are non-monotonic functions of the sample size, thus giving a hint about the complex nonlinearity characterizing this bending problem.

Fig. 9 shows the predicted size-effect by plotting the normalized bending moment M/h^2, where M is given by Eq. (71) with $\lambda=1$, as a function of the non-dimensional applied inner radius. These results are obtained by setting the rate $m_r=1$ of decrease of size-dependent hardening in Eq. (93) to be much smaller than the rate $m_\ell=15$ of increase of hardening. The qualitative behavior of GNDs is consistent with these parameters if their pile up is easier than their annihilation, as it should be due to the development of statistically stored dislocations (SSDs). The adopted non-vanishing value of m_r is however large enough to predict some softening that is observed at the end of the curve for $A/\ell=1$, which is due to the allowed recovery, caused by a reduction of ξ. By setting $m_r=0$ (not displayed for clarity of the figure) that decrease in the moment's magnitude, when the value of A for the inner radius

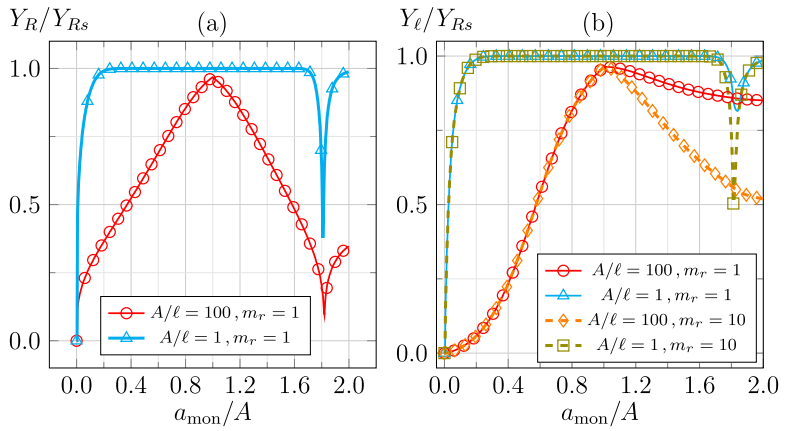

Fig. 10. Normalized size-dependent hardening variables at $R = A$, in the uniform bending of a circular sector with $B/A = 1.1$, $H/A = 0.1$, $\alpha_z = \pi/6$, for different values of the hardening parameter m_r as functions of the normalized monotonically increasing loading parameter $a_{\rm mon}/A$: the normalized current saturated value of the size-dependent hardening Y_R/Y_{Rs}, which is basically unaffected by m_r (not displayed in the figure) (a) and the normalized actual size-dependent hardening Y_ℓ/Y_{Rs} (b).

is almost recovered, disappears even though ξ is almost independent of m_r in this problem. On the contrary, increasing m_r towards m_ℓ makes that drop in the moment's magnitude larger.

The main result observed in Fig. 9 is, of course, the capability of the proposed theory to predict a significant size-effect encompassing both strengthening and increase in strain hardening with diminishing size. The fact that the observed size-effect spans about three orders of magnitude in sample size (note that the curve for $A/\ell = 1000$ is quite close to the case of conventional plasticity) is due to the chosen value for the material parameter $n_R = 0.3$.

The influence of m_r is highlighted in Fig. 10, displaying the evolutions of the size-dependent hardening variables Y_R and Y_ℓ. In order to more clearly illustrate the results, the evolution is provided as a function of the monotonically increasing loading parameter

$$a_{\rm mon} = \int_0^t |\dot{a}|\mathrm{d}t\,.$$

Given that in the considered loading history A is decreased to $A/100$ and it is then increased back to A, it turns out that $a_{\rm mon}/A \in [0, 1.98]$. The minimum value of inner radius is attained at time t_0, with the entire process, including reverse loading, lasting $2t_0$.

For graphical clarity, Fig. 10 focuses only on two sizes, namely $A/\ell = 1$ and $A/\ell = 100$, and on the inner radius, where, as illustrated later in Fig. 13, incompatibility is larger. From Fig. 10(a), it is observed that Y_R rapidly reaches its saturated value Y_{Rs} for $A/\ell = 1$ and, after reversing loading, it takes a while before this target value of the size-dependent hardening diminishes. This is mildly due to the material parameter $n_R = 0.3$ selected for the last relation of Eq. (93) and mainly due to the large values rapidly attained by $|\xi|$ for $A/\ell = 1$. Instead, for $A/\ell = 100$ the maximum saturated value Y_{Rs} is not reached at the end of the loading ramp (at $t = t_0$), such that a decrease of Y_R is almost immediately observed for $t > t_0$ because, once loading is reversed, plasticity is very soon resumed, as is clear from Fig. 9. Also, the legend of Fig. 10(a) specifies that the two curves there displayed are obtained for $m_r = 1$ even though, in fact, in the considered loading process Y_R is almost independent of m_r. Instead, the actual size-dependent hardening Y_ℓ in the sixth relation of Eq. (93) is, obviously, very much dependent on m_r. Fig. 10(b) considers $m_r = 1$ and $m_r = 10$. For the case $m_r = 10$, the rate of recovery is increased, causing Y_ℓ to follow Y_R more closely during recovery. This is evident for the case $A/\ell = 1$, in which the model response exhibits a stronger dependence on R_{23}; instead, for $A/\ell = 100$ variations in ξ are more limited, such that Y_ℓ experiences a delay in following Y_R. For instance, the increase of Y_R at about the end of the loading history that is observable in Fig. 10(a) has no clear counterpart in Fig. 10(b), where only a decrease of the, still negative, slope of the function $Y_\ell(a_{\rm mon})$ is observed. Still for the sake of graphical clarity, Fig. 10(b) does not include curves for $m_r = 0$, whose behavior is anyway easy to describe: in this case, in which hardening recovery is not allowed at all, the curves $Y_\ell(a_{\rm mon})$ may not decrease, such that when they reach the maxima displayed in Fig. 10(b) they remain flat. Of course, the general trend consists of faster recovery of size-dependent hardening with increasing m_r towards m_ℓ.

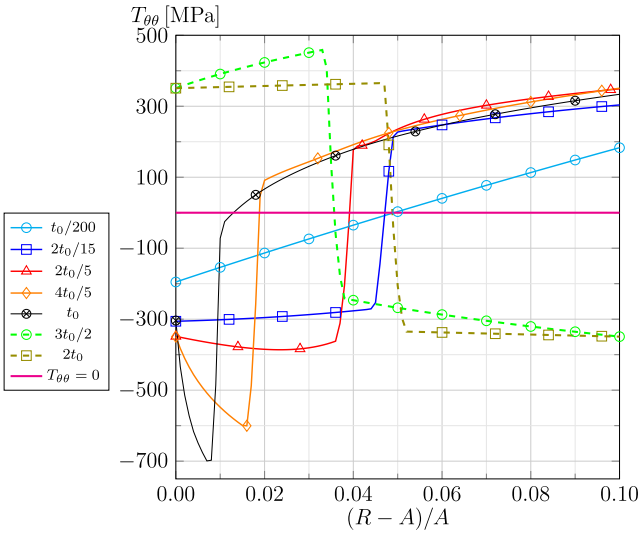

Fig. 11. Uniform bending of a circular sector with $B/A = 1.1$, $H/A = 0.1$, $\alpha_z = \pi/6$: Circumferential stress at $R = A$, $T_{\theta\theta}(R)$, for conventional plasticity ($A/\ell \to \infty$). t_0 is the fictitious time to complete a loading ramp, such that the whole analysis, including reverse loading, lasts $2t_0$. The zero-stress straight line indicating the neutral plane is plotted for reference.

One of the most interesting features of finite-deformation elasto-plastic bending is the evolution of the circumferential normal stress $T_{\theta\theta}$. This is illustrated in Figs. 11 and 12, considering, respectively, the extreme cases $A/\ell \to \infty$ (i.e. conventional plasticity) and $A/\ell = 1$. The evolution is represented by presenting the spatial distribution of $T_{\theta\theta}$ at various instants along the loading history, the selected instants being defined in terms of the time t_0.

The circumferential stress $T_{\theta\theta}$ is plotted, in Figs. 11 and 12, versus the non-dimensional Lagrangian coordinate $(R - A)/A$. The use of the Lagrangian coordinate allows for the appreciation of the large motion of the neutral plane (defined by $T_{\theta\theta} = 0$) through the material during the loading history. Given that, in this regard, the same behavior is observed in both Figs. 11 and 12 with similar amplitude, this effect is due to large deformations and geometry, irrespective of the sample

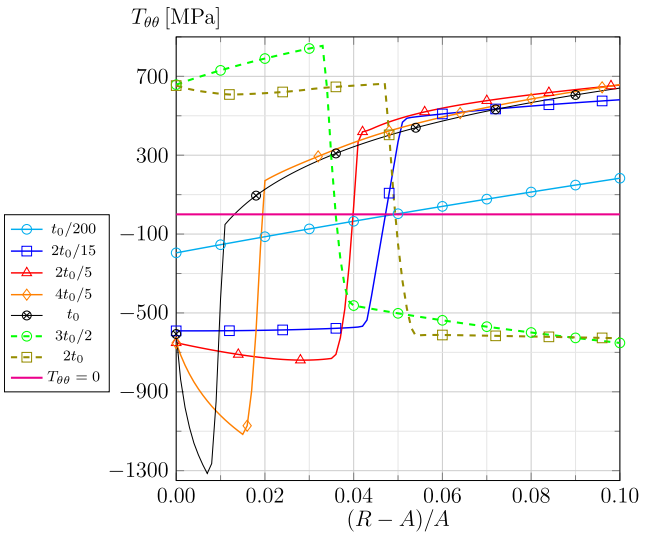

Fig. 12. Uniform bending of a circular sector with $B/A = 1.1$, $H/A = 0.1$, $\alpha_z = \pi/6$: Circumferential stress at $R = A$, $T_{\theta\theta}(R)$, for the smallest, i.e. stiffest, sample considered ($A/\ell = 1$). t_0 is the fictitious time to complete a loading ramp, such that the whole analysis lasts $2t_0$. The zero-stress straight line indicating the neutral plane is plotted for reference.

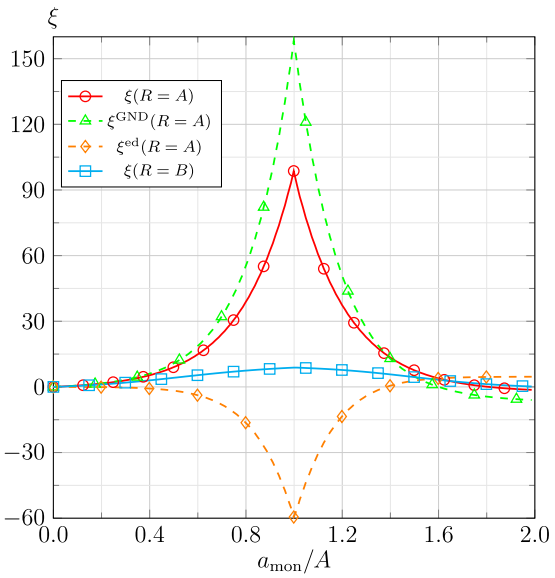

Fig. 13. Uniform bending of a circular sector with $B/A = 1.1$, $H/A = 0.1$, $\alpha_z = \pi/6$: The scalar field ξ governing the size-dependent hardening for the smallest, i.e. stiffest, sample considered ($A/\ell = 1$) at $R = A$ and $R = B$ as a function of the normalized monotonically increasing loading parameter $a_{\rm mon}/A$. The graph includes, for the point $R = A$ only, also the contributions to ξ due to densities of GNDs and to the elastic distortion of the crystal lattice.

size. Specifically, at the end of the loading ramp (black curve with circles in Figs. 11 and 12), the neutral plane ends up very close to the inner radius, corresponding to a starkly non-skew-symmetric stress distribution.

In contrast with the pure elastic behavior illustrated in Fig. 8(b), again for both cases $A/\ell \to \infty$ and $A/\ell = 1$, the maximum compressive stress, $T_{\theta\theta}^{\rm cmax}$, does not occur at the inner radius a. Additionally, the difference between $T_{\theta\theta}^{\rm cmax}$ and $T_{\theta\theta}(r = a)$ is very large at the end of the loading ramp. Note that this behavior holds also for conventional perfect plasticity (not displayed for brevity, as Fig. 11 includes conventional hardening) and can be explained as follows. At $r = a$, $T_{\theta\theta}$ is limited by the combination of three factors: the boundary condition $T_{rr}(r = a) = 0$, the incompressibility, and the saturation of the hardening variable, the latter being Y_{H_S} by for instance referring to the case $A/\ell \to \infty$ (Fig. 11). A simple analysis shows that, in the limit case of no overstress, $T_{\theta\theta}(r = a)$ results to be limited by the value $\approx 2\mu Y_{H_S}/\sin(2\alpha)$. When this value is reached at $r = a$ the magnitude of the compressive stress must increase in some other material points to ensure that the circumferential axial force remains null while the bending moment increases. This behavior, characterized by the peaks $T_{\theta\theta}^{\rm cmax}$ of compressive stress displayed in the red, orange, and black curves in Figs. 11 and 12, is emphasized by the motion of the neutral plane towards $r = a$. Note that the capability of $T_{\theta\theta}$ to exhibit those peaks corresponds to the largest pressure values in the same material points. Also, this behavior would be emphasized by decreasing A/B. It is remarked that the material point at $r = a$ experiences the largest circumferential deformation, consistently with the purely elastic behavior illustrated in Fig. 8(b). Moreover, by comparison of Figs. 11 and 12, it is noted that the main difference between the cases $A/\ell \to \infty$ and $A/\ell = 1$ consists of the much larger stress in the latter. For instance, at t_0, $T_{\theta\theta}^{\rm cmax}$ for $A/\ell = 1$ is almost double than $T_{\theta\theta}^{\rm cmax}$ for conventional plasticity. In summary, it is observed that the size-dependence has a huge effect on the stress amplitude, but, for the considered loading path, it has a limited impact on the qualitative behavior, whose specific features are related to the sector shape and to finite-deformation elastoplasticity.

The size-effect observed in Fig. 9, specifically involving both strengthening and increase in strain hardening with diminishing size, has, of course, to be ascribed to the evolution of ξ and to the ratio m_r/m_ℓ. Fig. 13 shows, for the smallest sample, $A/\ell = 1$, the evolution of ξ in the inner and outer radii.

The first observations, by comparing the curve for $\xi(R = A)$ (red) with that for $\xi(R = B)$ (cyan) in Fig. 13, are that incompatibility is larger at the inner radius, due to the largest gradients there, and that incompatibility has the same sign at inner and outer radii.

What is far less obvious, and constitutes a central result of this investigation, is that the two contributions to the rate of elastic incompatibility $R_{23}^{\rm GND}$ and $R_{23}^{\rm ed}$, that are due to rates of GNDs densities and elastic distortion of the crystal lattice, are of the same order of magnitude, thus being equally important. In Fig. 13, $\xi^{\rm ed}$ and $\xi^{\rm GND}$ are displayed with green-triangle and orange-diamond curves at the inner radius, where incompatibility is larger and the two contributions have opposite sign, as it can be deduced from inspection of Eq. (88). Specifically, the maximum values reached by $|\xi^{\rm ed}|$ and $|\xi^{\rm GND}|$ result $\approx$59.5 and $\approx$158.

Note that in this elastoplastic case, because of the material parameters selected in Eq. (98) for the conventional part of the model, the angle α has a very limited variation along the sector thickness. For instance, at the end of the loading, when $a = A/100$, in conventional perfect plasticity, α varies from 30.07° at $r = a$ to 29.93° at $r = b$, while in the case of hardening with $A/\ell = 1$, α varies from 30.18° at $r = a$ to 29.81° at $r = b$. This is in stark contrast with the results displayed in Fig. 7, related to very large elastic deformations, which are needed to observe a non-negligible gradient of α and are not relevant for metal plasticity. Therefore, the sole contribution that counts for the incompatibility due to the elastic distortion of the crystal lattice is the first addend of $R_{23}^{\rm ed}$ in Eq. (88), which is proportional to $\sin(2\alpha)/r$.

Third, note that for the adopted loading history the field ξ scales almost linearly with the sample size, which is the reason why Fig. 13 only reports the case $A/\ell = 1$. To observe more complex phenomena related to the evolution of defects, one should analyze more complex cyclic loading paths.

Figs. 14 and 15 report, for all the considered sample sizes, the residual stresses, $T_{\theta\theta}^{\rm res}$ and $T_{rr}^{\rm res}$, obtained at the instant when, during reverse loading, the bending moment vanishes. The residual stresses are plotted in Figs. 14 and 15 as functions of the current (non-dimensional) radial position, such that it may be easier to notice that $T_{\theta\theta}^{\rm res}$ is such that both the bending moment and the axial circumferential force vanish.

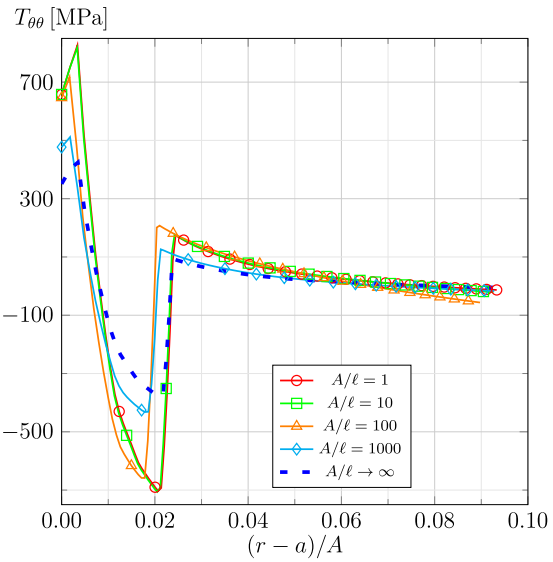

Fig. 14. Uniform bending of a circular sector with $B/A = 1.1$, $H/A = 0.1$, $\alpha_z = \pi/6$: Residual circumferential stress $T^{\text{res}}_{\theta\theta}$, for $M \approx 0$ during reverse loading, as a function of the normalized shifted current radial coordinate, at variable sample size.

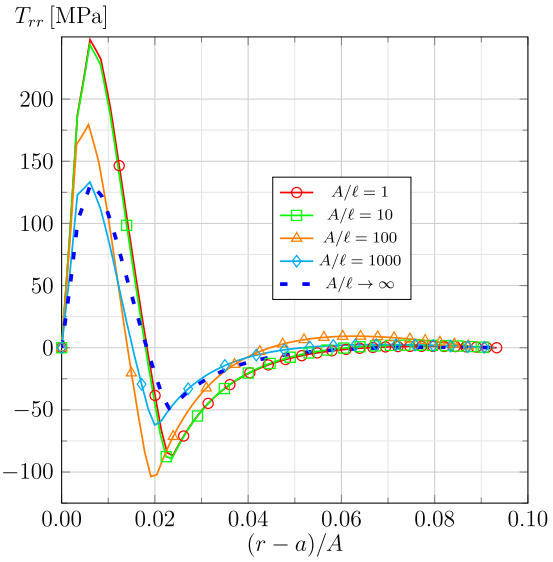

Fig. 15. Uniform bending of a circular sector with $B/A = 1.1$, $H/A = 0.1$, $\alpha_z = \pi/6$: Residual radial stress $T^{\text{res}}_{rr}(r)$, for $M \approx 0$ during reverse loading, as a function of the normalized shifted current radial coordinate, at variable sample size.

Of course, $T^{\text{res}}_{\theta\theta}$ and T^{res}_{rr} are interesting in this investigation because they are purely due to the incompatibility of the elastic deformation developed during loading and reverse loading up to $M = 0$. Again, it is observed that for the chosen loading path, the sample size has a negligible effect on the qualitative behavior, while it has an impact on the stress magnitude. From Figs. 14 and 15 it is also seen that the actual thickness h does not change much with the sample size.

5. Concluding remarks

This investigation leverages on (Rubin and Bardella, 2024) which introduces instantaneous Eulerian rates of elastic incompatibilities, denoted as R_{ij}, for anisotropic elastoplastic materials. The rates R_{ij} are highly nonlinear fields that depend on the constitutive equation for the plasticity rate tensor, $\mathbf{L}_p$, and particularize to the negative of the rate of the Nye-Kröner tensor (Nye, 1953; Kröner, 1962; Fleck and Hutchinson, 1997; Arsenlis and Parks, 1999) for small deformations. By definition, each component of R_{ij} is invariant under superposed rigid body motions such that it can be independently used in Eulerian constitutive equations (Rubin, 1994). While Rubin and Bardella (2024) discuss phenomenological elastoplasticity, here focus is on crystal plasticity.

The main obtained result is that, in crystal plasticity, the rates R_{ij} clearly display two distinct contributions to the elastic incompatibility, namely that due to rates of densities of geometrically necessary dislocations (GNDs, Ashby, 1970) and that due to the elastic distortion of the crystal lattice. The contribution due to GNDs is well-known, first, because it is the sole one playing a role in the framework of small strains and rotations; second, this contribution is the subject of several discussions in the literature on finite-deformation strain gradient plasticity (SGP) based on measures of incompatibility to model densities of GNDs, thus requiring the definition of Nye-Kröner-like tensors (see, e.g., Cermelli and Gurtin, 2001; Gurtin, 2006; Arora and Acharya, 2020; Rubin and Bardella, 2023, and references therein). However, the largest subclass of these SGP theories dealing with crystal plasticity relies on the multiplicative form $\mathbf{F} = \mathbf{F}_e\mathbf{F}_p$ and, noticeably, on *constant* crystallographic directions, which are usually defined in the intermediate configuration. Because of this, such a classical framework makes it difficult to clearly single out the contribution to the incompatibility due to the elastic distortion of the crystal lattice.

In this work, the roles played by the two foregoing contributions to R_{ij} are studied, first, by using R_{ij} to develop Eulerian hardening equations that include a size-dependence, also providing some latent hardening. By following (Rubin and Bardella, 2024), all the components of the rates R_{ij} are simply summed up and multiplied by a material length scale parameter, ℓ, into the equations for the size-dependent hardening, aiming at modeling generation and annihilation of defects of opposite sign.

Second, the proposed lower-order strain gradient crystal plasticity theory is applied to the large-deformation uniform bending of thick circular sectors subjected to loading and reverse loading. For a better understanding of the results, the bending response is discussed in detail also in the purely elastic regime. For elastoplasticity, this benchmark problem shows the capability of the proposed theory to predict size-effects typical of small-scale metal plasticity, including both strengthening and increase in strain hardening with diminishing size. Specifically, the prediction of the strengthening (i.e., an increase of the *apparent* yield point) is also possible because of the use of a smooth transition between the elastic and plastic regimes (Hollenstein et al., 2013, 2015). More importantly, the bending problem demonstrates that the contribution to R_{ij} due to the elastic distortion of the crystal lattice may have the same importance as that due to rates of densities of GNDs.

A limit of the adopted benchmark problem lies in its crystallography. In fact, in order to avoid too cumbersome computations, a symmetric double slip has been selected, thus hampering the development of the plastic spin rate $\mathbf{W}_p$. Future work should consider more complex boundary value problems, first of all adopting crystallography that allows for non-vanishing $\mathbf{W}_p$, as in the single slip case described in Appendix B. On the one hand, this is important for the crucial role $\mathbf{W}_p$ has on the incompatibility (Bardella, 2009; Bardella and Panteghini, 2015; Poh and Peerlings, 2016; Rubin and Bardella, 2024). On the other hand, this requires a more general numerical approach with respect to that followed in this investigation, for instance resorting to the finite element method. In this regard, note that strongly objective return mapping algorithms can be developed in the adopted Eulerian framework (see, e.g., Jabareen, 2015).

CRediT authorship contribution statement

Lorenzo Bardella: Writing – review & editing, Writing – original draft, Visualization, Validation, Software, Methodology, Investigation, Formal analysis, Data curation, Conceptualization. **M.B. Rubin:** Writing – review & editing, Writing – original draft, Methodology, Investigation, Formal analysis, Conceptualization. **Andrea Panteghini:** Writing – original draft, Software, Investigation, Visualization.

Declaration of competing interest

The authors declare that they have no known competing financial interests or personal relationships that could have appeared to influence the work reported in this paper.

Acknowledgments

L.B. and A.P. acknowledge the support of the Italian Ministry of Education, University, and Research (MIUR). This work was done under the auspice of GNFM (Gruppo Nazionale per la Fisica Matematica) of INDAM (Istituto Nazionale di Alta Matematica Francesco Severi).

Appendix A. Numerical implementation of the elastoplastic problem

First, it is useful to collect the equations to be solved for size-independent perfect plasticity ($m_H = \ell = 0$):

$$\text{Assign} \quad a(t) \quad \text{with} \quad a(t=0) = a_0 \equiv A\,,$$
$$\frac{1}{m'_{1r}}\frac{\partial m'_{1r}}{\partial a} = -\mathcal{F}(R,a) + \frac{\Gamma\sin(2\alpha)}{\dot a}\,,$$
$$m'_{1r}(R,a_0) = 1\,, \quad \beta(a_0) = 1\,,$$
$$\mathcal{F}(R,a) = \frac{a}{a^2+\frac{R^2-A^2}{\beta}} + \left(\frac{a^2}{a^2+\frac{R^2-A^2}{\beta}}+1\right)\frac{1}{2\beta}\frac{\mathrm{d}\beta}{\mathrm{d}a}\,,$$
$$\Gamma = b_\Gamma\left|\mathcal{F}(R,a)\dot a\sin(2\alpha)\right|\langle|\gamma_e| - Y\rangle\frac{\gamma_e}{|\gamma_e|}\,,$$
$$\alpha = \sin^{-1}\frac{\sin(\alpha_z)m'^2_{1r}}{\sqrt{\sin^2(\alpha_z)m'^4_{1r}+\cos^2(\alpha_z)}}\,, \quad \gamma_e = \frac{1-m'^4_{1r}}{2m'^2_{1r}}\sin(2\alpha)\,,$$
$$\frac{\partial T_{rr}}{\partial R} = \frac{\mu\left(\frac{1}{m'^2_{1r}} - m'^2_{1r}\right)R}{\beta a^2 + R^2 - A^2}\,, \quad T_{rr}(A,a(t)) = 0\,, \quad T_{rr}(B,a(t)) = 0\,.$$

Including hardening just consists of adding Eqs. (88), (92), (93). However, such an addition leads to a further, significant numerical complexity, as it requires iteration on the derivatives with respect to r involved in the definition of R_{23} in Eq. (88).

This numerical problem has been solved in this work by implementing a specific Fortran code, whose main features are described below.

In a generic loading increment t_{n+1}, the current value of the inner radius

$$a(t_{n+1}) \equiv a$$

is assigned. An explicit integration scheme for the hardening is assumed, such that, at each material point, the hardening value from the previous increment, $Y(R,t_n) \equiv Y_n$, is used to obtain the solution.

The solution at t_{n+1} can be found by imposing that $T_{rr}(B,a) = 0$. In fact, this condition becomes a nonlinear scalar equation in β that can be solved by using the Newton method, as explained in the following.

Given the current tentative value of β during a generic Newton's iteration, it is necessary to evaluate T_{rr} and its derivative with respect to β to determine the Newton's correction. At each material point R, the function $\mathcal{F}$ is computed by

$$\mathcal{F} = \frac{a}{a^2+\frac{R^2-A^2}{\beta}} + \left(\frac{a^2}{a^2+\frac{R^2-A^2}{\beta}}+1\right)\frac{1}{2\beta}\frac{\Delta\beta}{\Delta a}\,,$$

where the dependence of $\mathcal{F}$ on R and a has been dropped for simplicity and the standard notation

$$\Delta f = f - f_n \equiv f(t_{n+1}) - f(t_n)$$

is adopted.

The function m'_{1r} is computed at each material point by using a predictor–corrector integration scheme. Specifically, the implicit integration of Eq. (90) gives

$$m'_{1r} = \frac{m'_{1r,n}}{1+\Delta a\mathcal{F}+\Gamma\sin(2\alpha)\Delta t}\,, \tag{A.1}$$

where

$$\Delta t = \frac{\Delta a}{\dot a}\,,$$

whose magnitude plays no role in the present rate-independent model.

It is initially assumed that at the considered material point $\Gamma = 0$ to obtain the elastic trial values

$$m'^*_{1r} = \frac{m'_{1r,n}}{1+\Delta a\mathcal{F}}\,, \quad \alpha^* = \sin^{-1}\frac{\sin(\alpha_z)m'^{*2}_{1r}}{\sqrt{\sin^2(\alpha_z)m'^{*4}_{1r}+\cos^2(\alpha_z)}}\,,$$
$$\gamma^*_e = \frac{1-m'^{*4}_{1r}}{2m'^{*2}_{1r}}\sin(2\alpha^*)\,.$$

If $|\gamma^*_e| \le Y_n$ holds, the solution is acceptable and, for the considered material point, $m'_{1r} = m'^*_{1r}, \alpha = \alpha^*, \gamma_e = \gamma^*_e, \Gamma = 0$. Otherwise, the solution is unacceptable and m'_{1r} is then computed, at the material point, by solving the nonlinear scalar Eq. (A.1), with

$$\alpha = \sin^{-1}\frac{\sin(\alpha_z)m'^2_{1r}}{\sqrt{\sin^2(\alpha_z)m'^4_{1r}+\cos^2(\alpha_z)}}\,, \quad \gamma_e = \frac{1-m'^4_{1r}}{2m'^2_{1r}}\sin(2\alpha)\,,$$
$$\Gamma\Delta t = b_\Gamma\left|\Delta a\mathcal{F}\sin(2\alpha)\right|\left(|\gamma_e| - Y_n\right)\frac{\gamma_e}{|\gamma_e|}\,. \tag{A.2}$$

Once m'_{1r} is computed at all material points $R \in [A,B]$ for the current value of β, T_{rr} is evaluated by integrating, through the Simpson rule, Eq. (96) with $T_{rr}(A,a) = 0$. Then, the current value of β is acceptable if it results

$$\frac{|T_{rr}(B,a)|}{\mu Y_{H0}} \le \varepsilon\,,$$

where ε is a suitably small positive number that has been set equal to 10^{-12}. Otherwise, a new iteration on β must be carried out. The updated value of β simply is equal to

$$\beta - T_{rr}(B,a)\left[\frac{\partial T_{rr}}{\partial\beta}\Big|_{B,a}\right]^{-1}\,,$$

where the derivative $\partial T_{rr}/\partial\beta$ is computed numerically by suitably perturbing β. Once β has reached convergence, it is finally necessary to update the hardening variable $Y(t)$ for the next time step. The size-dependent hardening $Y_\ell(t)$ requires the spatial derivatives of α and Γ. To obtain them, Eqs. (A.1) and (A.2) are differentiated with respect to the space. These differentiated equations implicitly define the spatial derivatives of α and Γ, and can be solved by the Newton method, because the values of m'_{1r} and α at the end of the time step are at this stage of the algorithm known and $\partial\mathcal{F}/\partial R$ can be computed analytically.

The quality of the results has been checked by suitably refining both the time and the spatial discretizations.

Appendix B. The case of single slip

In this case, the following single slip system is considered

$${}_1\mathbf{s} = \sin(\alpha)\mathbf{e}_r + \cos(\alpha)\mathbf{e}_\theta\,, \quad {}_1\mathbf{n} = -\cos(\alpha)\mathbf{e}_r + \sin(\alpha)\mathbf{e}_\theta\,, \quad {}_1\mathbf{t} = \mathbf{e}_z\,. \tag{B.1}$$

It follows that the plastic rate in Eq. (7) specializes to

$$\mathbf{L}''_p = {}_1\Gamma[\sin(\alpha)\cos(\alpha)(-\mathbf{e}_r\otimes\mathbf{e}_r + \mathbf{e}_\theta\otimes\mathbf{e}_\theta) + \sin^2(\alpha)\mathbf{e}_r\otimes\mathbf{e}_\theta - \cos^2(\alpha)\mathbf{e}_\theta\otimes\mathbf{e}_r]\,, \tag{B.2}$$

which leads to

$$\mathbf{D}''_p = \frac{{}_1\Gamma}{2}[\sin(2\alpha)(-\mathbf{e}_r\otimes\mathbf{e}_r + \mathbf{e}_\theta\otimes\mathbf{e}_\theta) - \cos(2\alpha)(\mathbf{e}_r\otimes\mathbf{e}_\theta + \mathbf{e}_\theta\otimes\mathbf{e}_r)]\,,$$
$$\mathbf{W}_p = \frac{{}_1\Gamma}{2}(\mathbf{e}_r\otimes\mathbf{e}_\theta - \mathbf{e}_\theta\otimes\mathbf{e}_r)\,.$$

The form of the plastic rate in Eq. (B.2) for single slip breaks the symmetry that allows the distortional microstructural vectors to be written as in Eq. (57). In this case and under plane strain, they instead have the form

$$\begin{aligned}&\mathbf{m}'_1 = m'_{1r}\mathbf{e}_r + m'_{1\theta}\mathbf{e}_\theta\,, \quad \mathbf{m}'_2 = m'_{2r}\mathbf{e}_r + m'_{2\theta}\mathbf{e}_\theta\,, \quad \mathbf{m}'_3 = \mathbf{e}_z\,,\\ &m'_{1r}m'_{2\theta} - m'_{2r}m'_{1\theta} = 1\,,\\ &\mathbf{m}^{1\prime} = m'_{2\theta}\mathbf{e}_r - m'_{2r}\mathbf{e}_\theta\,, \quad \mathbf{m}^{2\prime} = -m'_{1\theta}\mathbf{e}_r + m'_{1r}\mathbf{e}_\theta\,, \quad \mathbf{m}^{3\prime} = \mathbf{e}_z\,.\end{aligned} \tag{B.3}$$

From Eqs. (28) and (B.3),

$$\begin{aligned}\mathbf{B}'_e &= (m'^2_{1r} + m'^2_{2r})\mathbf{e}_r\otimes\mathbf{e}_r + (m'^2_{1\theta} + m'^2_{2\theta})\mathbf{e}_\theta\otimes\mathbf{e}_\theta + \mathbf{e}_z\otimes\mathbf{e}_z\\ &\quad + (m'_{1r}m'_{1\theta} + m'_{2r}m'_{2\theta})(\mathbf{e}_r\otimes\mathbf{e}_\theta + \mathbf{e}_\theta\otimes\mathbf{e}_r)\,,\\ \mathbf{B}''_e &= \Big[\frac{2}{3}(m'^2_{1r} + m'^2_{2r}) - \frac{1}{3}(m'^2_{1\theta} + m'^2_{2\theta}) - \frac{1}{3}\Big]\mathbf{e}_r\otimes\mathbf{e}_r\\ &\quad + \Big[-\frac{1}{3}(m'^2_{1r} + m'^2_{2r}) + \frac{2}{3}(m'^2_{1\theta} + m'^2_{2\theta}) - \frac{1}{3}\Big]\mathbf{e}_\theta\otimes\mathbf{e}_\theta\\ &\quad + \Big[-\frac{1}{3}(m'^2_{1r} + m'^2_{2r}) - \frac{1}{3}(m'^2_{1\theta} + m'^2_{2\theta}) + \frac{2}{3}\Big]\mathbf{e}_z\otimes\mathbf{e}_z\\ &\quad + (m'_{1r}m'_{1\theta} + m'_{2r}m'_{2\theta})(\mathbf{e}_r\otimes\mathbf{e}_\theta + \mathbf{e}_\theta\otimes\mathbf{e}_r)\,,\\ {}_1\gamma_e &= \sin(\alpha)\cos(\alpha)(-m'^2_{1r} - m'^2_{2r} + m'^2_{1\theta} + m'^2_{2\theta}) - \cos(2\alpha)(m'_{1r}m'_{1\theta} + m'_{2r}m'_{2\theta})\,,\\ \frac{\partial T_{rr}}{\partial r} &= \frac{\mu}{r}\Big(-m'^2_{1r} - m'^2_{2r} + m'^2_{1\theta} + m'^2_{2\theta}\Big)\,.\end{aligned}$$

The non-vanishing shear stress $T_{r\theta} = \mu(m'_{1r}m'_{1\theta} + m'_{2r}m'_{2\theta})$ makes this boundary value problem two-dimensional, being then much harder to solve than that characterized by the symmetric double slip of Section 4.4.

It is, however, possible and interesting to obtain the forms of the Eulerian rates of elastic incompatibilities for the case of single slip. By using Eqs. (9) and (57) and by taking $\alpha = \alpha_z$ in a RLS, from Eqs. (B.1) and (B.3) it follows that

$$\begin{aligned}&{}_1s^1 = \sin(\alpha_z)\,, \quad {}_1s^2 = \cos(\alpha_z)\,, \quad {}_1s^3 = 0\,,\\ &{}_1n_1 = -\cos(\alpha_z)\,, \quad {}_1n_2 = \sin(\alpha_z)\,, \quad {}_1n_3 = 0\,,\\ &{}_1\mathbf{s} = \frac{[\sin(\alpha_z)m'_{1r} + \cos(\alpha_z)m'_{2r}]\mathbf{e}_r + [\sin(\alpha_z)m'_{1\theta} + \cos(\alpha_z)m'_{2\theta}]\mathbf{e}_\theta}{\sqrt{[\sin(\alpha_z)m'_{1r} + \cos(\alpha_z)m'_{2r}]^2 + [\sin(\alpha_z)m'_{1\theta} + \cos(\alpha_z)m'_{2\theta}]^2}}\,,\\ &{}_1\mathbf{n} = \frac{[-\sin(\alpha_z)m'_{1\theta} - \cos(\alpha_z)m'_{2\theta}]\mathbf{e}_r + [\cos(\alpha_z)m'_{2r} + \sin(\alpha_z)m'_{1r}]\mathbf{e}_\theta}{\sqrt{[\sin(\alpha_z)m'_{1\theta} + \cos(\alpha_z)m'_{2\theta}]^2 + [\cos(\alpha_z)m'_{2r} + \sin(\alpha_z)m'_{1r}]^2}}\,,\\ &{}_1\mathbf{t} = \mathbf{e}_z\,, \quad \sin(\alpha) = {}_1\mathbf{s}\cdot\mathbf{e}_r\,.\end{aligned}$$

Because of Eq. (B.1), Eq. (17) specializes to

$$\begin{aligned}&{}_1\Gamma\,\mathrm{curl}({}_1\mathbf{s}\otimes{}_1\mathbf{n}) = {}_1\Gamma[{}_1\mathbf{s}\otimes\mathrm{curl}({}_1\mathbf{n}) + (\partial_1\mathbf{s}/\partial\mathbf{x})({}_1\mathbf{s}\otimes\mathbf{e}_z - \mathbf{e}_z\otimes{}_1\mathbf{s})]\\ &= {}_1\Gamma\left[\left(\frac{\sin^2(\alpha)}{r} + \sin(2\alpha)\frac{\partial\alpha}{\partial r}\right)\mathbf{e}_r + \left(\frac{\sin(2\alpha)}{2r} + \cos(2\alpha)\frac{\partial\alpha}{\partial r}\right)\mathbf{e}_\theta\right]\otimes\mathbf{e}_z\,.\end{aligned} \tag{B.4}$$

The contribution to $\mathrm{curl}(\mathbf{L}_p)$ in Eq. (16) due to pure densities of edge GNDs reads

$${}_1\dot\rho_{\perp1}\mathbf{s}\otimes{}_1\mathbf{t} = \frac{\partial_1\Gamma}{\partial r}\sin(\alpha)[\sin(\alpha)\mathbf{e}_r\otimes\mathbf{e}_z + \cos(\alpha)\mathbf{e}_\theta\otimes\mathbf{e}_z]\,. \tag{B.5}$$

Thus, summing up Eqs. (B.4) and (B.5), one obtains, for the single slip here concerned,

$$\begin{aligned}\mathrm{curl}(\mathbf{L}_p) &= \left[{}_1\Gamma\left(\frac{\sin^2(\alpha)}{r} + \sin(2\alpha)\frac{\partial\alpha}{\partial r}\right) + \frac{\partial_1\Gamma}{\partial r}\sin^2(\alpha)\right]\mathbf{e}_r\otimes\mathbf{e}_z\\ &\quad + \left[{}_1\Gamma\left(\frac{\sin(2\alpha)}{2r} + \cos(2\alpha)\frac{\partial\alpha}{\partial r}\right) + \frac{1}{2}\frac{\partial_1\Gamma}{\partial r}\sin(2\alpha)\right]\mathbf{e}_\theta\otimes\mathbf{e}_z\,.\end{aligned} \tag{B.6}$$

By combining Eqs. (3), (B.6), and (B.3), the non-vanishing Eulerian rates of elastic incompatibilities have the forms

$$\begin{aligned}R_{13} &= \left[{}_1\Gamma\left(\frac{\sin^2(\alpha)}{r} + \sin(2\alpha)\frac{\partial\alpha}{\partial r}\right) + \frac{\partial_1\Gamma}{\partial r}\sin^2(\alpha)\right]m'_{1r}m'_{3z}\\ &\quad + \left[{}_1\Gamma\left(\frac{\sin(2\alpha)}{2r} + \cos(2\alpha)\frac{\partial\alpha}{\partial r}\right) + \frac{1}{2}\frac{\partial_1\Gamma}{\partial r}\sin(2\alpha)\right]m'_{1\theta}m'_{3z}\,,\\ R_{23} &= \left[{}_1\Gamma\left(\frac{\sin^2(\alpha)}{r} + \sin(2\alpha)\frac{\partial\alpha}{\partial r}\right) + \frac{\partial_1\Gamma}{\partial r}\sin^2(\alpha)\right]m'_{2r}m'_{3z}\\ &\quad + \left[{}_1\Gamma\left(\frac{\sin(2\alpha)}{2r} + \cos(2\alpha)\frac{\partial\alpha}{\partial r}\right) + \frac{1}{2}\frac{\partial_1\Gamma}{\partial r}\sin(2\alpha)\right]m'_{2\theta}m'_{3z}\,.\end{aligned}$$

Also, differentiating Eq. (B.3) leads to

$$\begin{aligned}\dot{\mathbf{m}}'_1 &= \dot m'_{1r}\mathbf{e}_r + \frac{\dot\beta}{\beta}\theta m'_{1r}\mathbf{e}_\theta + \dot m'_{1\theta}\mathbf{e}_\theta - \frac{\dot\beta}{\beta}\theta m'_{1\theta}\mathbf{e}_r\,,\\ \dot{\mathbf{m}}'_2 &= \dot m'_{2r}\mathbf{e}_r + \frac{\dot\beta}{\beta}\theta m'_{2r}\mathbf{e}_\theta + \dot m'_{2\theta}\mathbf{e}_\theta - \frac{\dot\beta}{\beta}\theta m'_{2\theta}\mathbf{e}_r\,,\end{aligned}$$

that should be combined with the general evolution equation in (5), the expression for the total velocity gradient for this case, and Eq. (B.2) to obtain evolution equations for the distortional microstructural vectors under the initial conditions

$$m'_{1r}(r,0) = 1\,, \quad m'_{1\theta}(r,0) = 0\,, \quad m'_{2r}(r,0) = 0\,, \quad m'_{2\theta}(r,0) = 1\,.$$

Boundary value problems like this one are however better solved by using two-dimensional finite elements.

Data availability

Data will be made available on request.

References

Acharya, A., Bassani, J., 2000. Lattice incompatibility and a gradient theory of crystal plasticity. J. Mech. Phys. Solids 48 (8), 1565–1595. http://dx.doi.org/10.1016/S0022-5096(99)00075-7.

Amouzou-Adoun, Y.A., Jebahi, M., Forest, S., Fivel, M., 2024. Advanced modeling of higher-order kinematic hardening in strain gradient crystal plasticity based on discrete dislocation dynamics. J. Mech. Phys. Solids 193, 105875. http://dx.doi.org/10.1016/j.jmps.2024.105875.

Arora, R., Acharya, A., 2020. Dislocation pattern formation in finite deformation crystal plasticity. Int. J. Solids Struct. 184, 114–135. http://dx.doi.org/10.1016/j.ijsolstr.2019.02.013.

Arsenlis, A., Parks, D.M., 1999. Crystallographic aspects of geometrically-necessary and statistically-stored dislocation density. Acta Mater. 47 (5), 1597–1611. http://dx.doi.org/10.1016/S1359-6454(99)00020-8.

Asaro, R.J., 1983. Crystal plasticity. J. Appl. Mech.- Trans. ASME 50, 921–934. http://dx.doi.org/10.1115/1.3167205.

Ashby, M.F., 1970. The deformation of plastically non-homogeneous materials. Phil. Mag. 21, 399–424. http://dx.doi.org/10.1080/14786437008238426.

Bardella, L., 2006. A deformation theory of strain gradient crystal plasticity that accounts for geometrically necessary dislocations. J. Mech. Phys. Solids 54 (1), 128–160. http://dx.doi.org/10.1016/j.jmps.2005.08.003.

Bardella, L., 2009. A comparison between crystal and isotropic strain gradient plasticity theories with accent on the role of the plastic spin. Eur. J. Mech. A- Solid 28 (3), 638–646. http://dx.doi.org/10.1016/j.euromechsol.2008.10.006.

Bardella, L., Panteghini, A., 2015. Modelling the torsion of thin metal wires by distortion gradient plasticity. J. Mech. Phys. Solids 78, 467–492. http://dx.doi.org/10.1016/j.jmps.2015.03.003.

Bardella, L., Segurado, J., Panteghini, A., Llorca, J., 2013. Latent hardening size effect in small-scale plasticity. Modelling Simul. Mater. Sci. Eng. 21 (5), 055009. http://dx.doi.org/10.1088/0965-0393/21/5/055009.

Bilby, B.A., Gardner, L.R.T., Stroh, A.N., 1957. Continuous distributions of dislocations and the theory of plasticity. In: Proceedings of the 9th International Congress of Applied Mechanics. Vol. 9, University de Brussels, pp. 35–44.

Cermelli, P., Gurtin, M.E., 2001. On the characterization of geometrically necessary dislocations in finite plasticity. J. Mech. Phys. Solids 49 (7), 1539–1568. http://dx.doi.org/10.1016/S0022-5096(00)00084-3.

Engelen, R., Fleck, N., Peerlings, R., Geers, M., 2006. An evaluation of higher-order plasticity theories for predicting size effects and localisation. Int. J. Solids Struct. 43 (7), 1857–1877. http://dx.doi.org/10.1016/j.ijsolstr.2004.05.072.

Fleck, N.A., Hutchinson, J.W., 1997. Strain gradient plasticity. Adv. Appl. Mech. 33, 295–361.

Fleck, N.A., Hutchinson, J.W., Willis, J.R., 2014. Strain gradient plasticity under non-proportional loading. Proc. R. Soc. A 470, 20140267. http://dx.doi.org/10.1098/rspa.2014.0267.

Forest, S., Rubin, M., 2016. A rate-independent crystal plasticity model with a smooth elastic-plastic transition and no slip indeterminacy. Eur. J. Mech. A- Solid 55, 278–288. http://dx.doi.org/10.1016/j.euromechsol.2015.08.012.

Gambin, W., 1992. Refined analysis of elastic-plastic crystals. Int. J. Solids Struct. 29, 2013–2021. http://dx.doi.org/10.1016/0020-7683(92)90191-U.

Green, A.E., Zerna, W., 1954. Theoretical Elasticity. University Press, Oxford.

Gudmundson, P., 2004. A unified treatment of strain gradient plasticity. J. Mech. Phys. Solids 52, 1379–1406. http://dx.doi.org/10.1016/j.jmps.2003.11.002.

Gurtin, M.E., 2000. On the plasticity of single crystals: free energy, microforces, plastic-strain gradients. J. Mech. Phys. Solids 48 (5), 989–1036. http://dx.doi.org/10.1016/S0022-5096(99)00059-9.

Gurtin, M.E., 2004. A gradient theory of small-deformation isotropic plasticity that accounts for the Burgers vector and for dissipation due to plastic spin. J. Mech. Phys. Solids 52, 2545–2568. http://dx.doi.org/10.1016/j.jmps.2004.04.010.

Gurtin, M.E., 2006. The Burgers vector and the flow of screw and edge dislocations in finite-deformation single-crystal plasticity. J. Mech. Phys. Solids 54 (9), 1882–1898. http://dx.doi.org/10.1016/j.jmps.2006.03.003.

Gurtin, M.E., Anand, L., Lele, S.P., 2007. Gradient single-crystal plasticity with free energy dependent on dislocation densities. J. Mech. Phys. Solids 55 (9), 1853–1878. http://dx.doi.org/10.1016/j.jmps.2007.02.006.

Gurtin, M.E., Needleman, A., 2005. Boundary conditions in small-deformation, single-crystal plasticity that account for the Burgers vector. J. Mech. Phys. Solids 53 (1), 1–31. http://dx.doi.org/10.1016/j.jmps.2004.06.006.

Haouala, S., Lucarini, S., LLorca, J., Segurado, J., 2020. Simulation of the hall-petch effect in FCC polycrystals by means of strain gradient crystal plasticity and FFT homogenization. J. Mech. Phys. Solids 134, 103755. http://dx.doi.org/10.1016/j.jmps.2019.103755.

Havner, K.S., 1992. Finite Plastic Deformation of Crystalline Solids. In: Cambridge Monographs on Mechanics and Applied Mathematics, Cambridge University Press, Cambridge.

Hollenstein, M., Jabareen, M., Rubin, M.B., 2013. Modeling a smooth elastic–inelastic transition with a strongly objective numerical integrator needing no iteration. Comput. Mech. 52, 649–667. http://dx.doi.org/10.1007/s00466-013-0838-7.

Hollenstein, M., Jabareen, M., Rubin, M.B., 2015. Erratum to: Modeling a smooth elastic–inelastic transition with a strongly objective numerical integrator needing no iteration. Comput. Mech. 55, http://dx.doi.org/10.1007/s00466-014-1099-9, 453–453.

Hull, D., Bacon, D., 2001. Introduction to Dislocations, fourth ed. Butterworth-Heinemann, Oxford.

Idiart, M., Deshpande, V., Fleck, N., Willis, J., 2009. Size effects in the bending of thin foils. Internat. J. Engrg. Sci. 47 (11), 1251–1264. http://dx.doi.org/10.1016/j.ijengsci.2009.06.002.

Jabareen, M., 2015. Strongly objective numerical implementation and generalization of a unified large inelastic deformation model with a smooth elastic–inelastic transition. Internat. J. Engrg. Sci. 96, 46–67. http://dx.doi.org/10.1016/j.ijengsci.2015.07.001.

Kröner, E., 1959. General continuum theory of dislocations and intrinsic stresses. Arch. Ration. Mech. Anal. 4, 273–334. http://dx.doi.org/10.1007/BF00281393.

Kröner, E., 1962. Dislocations and continuum mechanics. Appl. Mech. Rev. 15, 599–606.

Lee, E.H., 1969. Elastic-plastic deformation at finite strains. J. Appl. Mech. 36, 1–6. http://dx.doi.org/10.1115/1.3564580.

Martínez-Pañeda, E., Niordson, C., Bardella, L., 2016. A finite element framework for distortion gradient plasticity with applications to bending of thin foils. Int. J. Solids Struct. 96, 288–299. http://dx.doi.org/10.1016/j.ijsolstr.2016.06.001.

Needleman, A., 2024. A perspective on plasticity, dissipation and the second law of thermodynamics. J. Appl. Mech.- Trans. ASME 91 (6), 061003. http://dx.doi.org/10.1115/1.4064700.

Niordson, C.F., Hutchinson, J.W., 2003. On lower order strain gradient plasticity theories. Eur. J. Mech. A- Solid 22 (6), 771–778. http://dx.doi.org/10.1016/S0997-7538(03)00069-X.

Nye, J.F., 1953. Some geometrical relations in dislocated crystals. Acta Metall. 1, 153–162. http://dx.doi.org/10.1016/0001-6160(53)90054-6.

Onat, E., 1968. The notion of state and its implications in thermodynamics of inelastic solids. In: Irreversible Aspects of Continuum Mechanics and Transfer of Physical Characteristics in Moving Fluids: Symposia Vienna, June 22–28, 1966. pp. 292–314.

Panteghini, A., Bardella, L., 2020. Modelling the cyclic torsion of polycrystalline micron-sized copper wires by distortion gradient plasticity. Phil. Mag. 100 (18), 2352–2364. http://dx.doi.org/10.1080/14786435.2020.1766144.

Panteghini, A., Bardella, L., Niordson, C.F., 2019. A potential for higher-order phenomenological strain gradient plasticity to predict reliable response under non-proportional loading. Proc. R. Soc. A 475 (2229), 20190258. http://dx.doi.org/10.1098/rspa.2019.0258.

Panteghini, A., Bardella, L., Rubin, M., 2025. Modeling yield stress scaling and cyclic response using a size-dependent theory with two plasticity rate fields. J. Mech. Phys. Solids 194, 105930. http://dx.doi.org/10.1016/j.jmps.2024.105930.

Poh, L.H., Peerlings, R.H.J., 2016. The plastic rotation effect in an isotropic gradient plasticity model for applications at the meso scale. Int. J. Solids Struct. 78–79, 57–69. http://dx.doi.org/10.1016/j.ijsolstr.2015.09.017.

Rice, J.R., 1971. Inelastic constitutive relations for solids: an internal-variable theory and its application to metal plasticity. J. Mech. Phys. Solids 19 (6), 433–455. http://dx.doi.org/10.1016/0022-5096(71)90010-X.

Rubin, M.B., 1994. Plasticity theory formulated in terms of physically based microstructural variables – Part I. Theory. Int. J. Solids Struct. 31, 2615–2634. http://dx.doi.org/10.1016/0020-7683(94)90222-4.

Rubin, M.B., 2012. Removal of unphysical arbitrariness in constitutive equations for elastically anisotropic nonlinear elastic–viscoplastic solids. Internat. J. Engrg. Sci. 53, 38–45. http://dx.doi.org/10.1016/j.ijengsci.2011.12.008.

Rubin, M.B., 2021. Continuum Mechanics with Eulerian Formulations of Constitutive Equations. Springer Nature.

Rubin, M., Bardella, L., 2023. An Eulerian thermodynamical formulation of size-dependent plasticity. J. Mech. Phys. Solids 170, 105122. http://dx.doi.org/10.1016/j.jmps.2022.105122.

Rubin, M., Bardella, L., 2024. Eulerian rates of elastic incompatibilities applied to size-dependent hardening in finite torsion. J. Mech. Phys. Solids 193, 105905. http://dx.doi.org/10.1016/j.jmps.2024.105905.

Stölken, J.S., Evans, A.G., 1998. A microbend test method for measuring the plasticity length scale. Acta Mater. 46, 5109–5115. http://dx.doi.org/10.1016/S1359-6454(98)00153-0.

Zecevic, M., Lebensohn, R.A., Capolungo, L., 2023. Non-local large-strain FFT-based formulation and its application to interface-dominated plasticity of nano-metallic laminates. J. Mech. Phys. Solids 173, 105187. http://dx.doi.org/10.1016/j.jmps.2022.105187.